

**NONINVASIVE IMAGING OF BRAIN VASCULATURE WITH HIGH
RESOLUTION BLOOD OXYGENATION LEVEL-DEPENDENT
VENOGRAPHY IN MAGNETIC RESONANCE IMAGING:
APPLICATIONS TO FUNCTIONAL AND CLINICAL STUDIES**

by

Sung-Hong Park

B. S. in Electrical Engineering, KAIST, South Korea, 1995

M.S. in Electrical Engineering, KAIST, South Korea, 1998

Submitted to the Graduate Faculty of
Swanson School of Engineering in partial fulfillment
of the requirements for the degree of
PhD in Bioengineering

University of Pittsburgh

2009

UNIVERSITY OF PITTSBURGH
SWANSON SCHOOL OF ENGINEERING

This dissertation was presented

by

Sung-Hong Park

It was defended on

April 10, 2009

and approved by

Edwin Nemoto, PhD, Professor in Radiology

George Stetten, MD/PhD, Professor in Bioengineering

QiuHong He, PhD, Associate Professor in Radiology and Bioengineering

Dissertation Director : Kyongtae Ty Bae, MD/PhD, Professor in Radiology

and Bioengineering

Copyright © by Sung-Hong Park

2009

**NONINVASIVE IMAGING OF BRAIN VASCULATURE WITH HIGH RESOLUTION BLOOD
OXYGENATION LEVEL-DEPENDENT VENOGRAPHY IN MAGNETIC RESONANCE
IMAGING: APPLICATIONS TO FUNCTIONAL AND CLINICAL STUDIES**

Sung-Hong Park, PhD

University of Pittsburgh, 2009

BOLD techniques have been used in a vast range of applications including functional MRI (fMRI) and clinical MR venography of brain vasculature. Despite the immense success of BOLD fMRI applications, our understanding of complex neuronal and hemodynamic processes associated with BOLD techniques is limited. An experimental investigation with BOLD MR venography may allow us to expand our knowledge in hemodynamic process involved in BOLD fMRI. BOLD techniques are also clinically useful. In clinical brain imaging studies, imaging both time-of-flight (TOF) MR angiogram (MRA) and BOLD MR venogram (MRV) is often desirable, because they complement the depiction of vascular pathologies. Nevertheless, MRV is usually not acquired to minimize the image acquisition time. It will be highly beneficial if we can acquire MRV while imaging MRA without increasing scan time. Thus, the objective of our study was to develop and assess BOLD MRV techniques for both functional and clinical applications.

For the experimental evaluation of BOLD MRV, we used a rat brain model at 9.4T. The scan condition for BOLD MRV was optimized and the venous origin of hypointense vasculature was investigated with modulation of oxygenation. Detailed

venules of ~16–30 μm diameter were detected in the resulting *in vivo* images with 78- μm isotropic scan resolution, verified with *in vivo* two-photon microscopy and computer simulation data. Activation foci of high-resolution BOLD fMRI maps were correlated with relatively large intracortical veins detected with high-resolution BOLD MRV, indicating that detectability of conventional BOLD fMRI is limited by density of these intracortical veins (~1.5 vessels/ mm^2).

For the clinical application of BOLD MRV, we developed and tested a compatible dual-echo arteriovenography (CODEA) technique for simultaneous acquisition of TOF MRA and BOLD MRV at a 3T human system. Image quality of the CODEA technique acquired in a single session was comparable to conventional TOF MRA and BOLD MRV separately acquired in two sessions. The CODEA technique was applied to chronic stroke studies. Detailed vascular structures including arterial occlusions and venous abnormalities were depicted. The CODEA technique appears valuable to other clinical applications, particularly for those requiring efficient MRA/MRV imaging with limited scan time such as acute stroke studies.

TABLE OF CONTENTS

1.0 INTRODUCTION	1
1.1 REVIEW OF TOF MR ANGIOGRAPHY AND BOLD MR VENOGRAPHY	1
1.1.1 TOF MR Angiography	2
1.1.2 BOLD MR Venography	8
1.2 STATEMENT OF PROBLEM	12
2.0 IMAGING BRAIN VASCULATURE WITH BLOOD OXYGENATION LEVEL-DEPENDENT MICROSCOPY: MR DETECTIN LIMITS DETERMINED BY IN VIVO TWO-PHOTON MICROSCOPY	14
2.1 INTRODUCTION	14
2.2 METHODS	16
2.2.1 Animal preparation	16
2.2.2 MRI Studies	17
2.2.2.1 Data collection	17
2.2.2.2 General venographic reconstruction, display, and SNR determination	18
2.2.2.3 Reconstruction of flattened cortical planes	19
2.2.2.4 Depth-dependent quantification of venous parameters	20

2.2.3 Two-photon Microscopy Studies	21
2.3 RESULTS	22
2.3.1 MRI Studies	22
2.3.1.1 TE-dependent studies	22
2.3.1.2 Oxygenation-dependent studies	25
2.3.1.3 Visualization of veins	27
2.3.1.4 Cortical depth-dependent venous distribution	29
2.3.2 Two-photon Microscopy Studies	32
2.4 DISCUSSION	34
2.4.1 Contrast in BOLD venograms	34
2.4.2 Threshold level for venous identification	35
2.4.3 Minimum-detectable Vessel Size in BOLD Microscopy	35
3.0 COMPATIBLE DUAL-ECHO ARTERIOVENOGRAPHY (CODEA) USING AN ECHO-SPECIFIC K-SPACE REORDERING SCHEME BASED ON TIME-OF-FLIGHT (TOF) AND BLOOD OXYGENATION LEVEL-DEPENDENT (BOLD) EFFECTS	39
3.1 INTRODUCTION	39
3.2 THEORY	41
3.2.1 Excitation RF pulses	41
3.2.2 CODEA with echo-specific K-space reordering scheme	43
3.3 METHODS	46

3.3.1	Single-slab, dual-echo arteriovenography (CODEA)	46
3.3.2	Conventional single-slab, single-echo MR angiography and MR venography	47
3.3.3	Multi-slab CODEA	47
3.3.4	Multi-slab, dual-echo arteriovenography without K-space reordering	48
3.3.5	Single-slab CODEA with MTC pulse	49
3.3.6	Reconstruction and data analysis	49
3.4	RESULTS	50
3.4.1	Single-slab CODEA MRA/MRV vs Conventional single-slab, single-echo MRA/MRV	50
3.4.2	Multi-slab CODEA MRA/MRV vs Multi-slab dual-echo MRA/MRV without K-space reordering	53
3.4.3	Single-slab CODEA MRA/MRV with MTC pulse	55
3.5	DISCUSSION	57
4.0	APPLICATIONS OF BLOOD OXYGENATION LEVEL-DEPENDENT MICROSCOPY AND COMPATIBLE DUAL-ECHO ARTERIOVENOGRAPHY (CODEA) TO FUNCTIONAL AND CLINICAL STUDIES	60
4.1	IMPLICATIONS OF BOLD MRV FOR BOLD FMRI	60
4.1.1	Introduction	60
4.1.2	Methods	61
4.1.3	Results and Discussion	62
4.2	APPLICATIONS OF COMPATIBLE DUAL-ECHO ARTERIOVENOGRAPHY (CODEA) IN STROKE	64

4.2.1 Introduction	64
4.2.2 Methods	65
4.2.3 Results	67
4.2.4 Discussion	69
5.0 SUMMARY AND CONCLUSIONS	71
APPENDIX A. COMPUTER SIMULATION STUDIES WITH A NUMERICAL SOLUTION OF BLOCH EQUATIONS FOR INVESTIGATION OF EXCITATION RF PULSE PROFILE USED IN TOF MR ANGIOGRAPHY AND COMPATIBLE DUAL- ECHO ARTERIOVENOGRAPHY (CODEA)	73
APPENDIX B. COMPUTER SIMULATION STUDIES WITH TWO- COMPARTMENT MODEL FOR EXAMINATION OF DETECTABILITY OF 9.4T BOLD MICROSCOPY	76
APPENDIX C. CONTRIBUTORS TO THE WORKS	79
BIBLIOGRAPHY	83

LIST OF FIGURES

- 1.1 **A schematic diagram illustrating the time-of-flight effect on MR signal intensities of moving blood and stationary tissue.** MR signal intensity of a fresh blood is unsaturated and higher than that of the saturated stationary tissue. However, after entering the imaging slab, blood spins experience increased number of RF excitations and lose signal intensity, as they flow to the opposite side of the slab. 4
- 1.2 **Shape and profile of RF pulse for TOF MRA. a:** Shapes of real and imaginary parts of symmetric RF pulse. **b:** Corresponding ramped excitation RF pulse profile. The flip angle ranges from 20° to 30° 4
- 1.3 **Shape and profile of Minimum-phase Shinnar-Le Roux excitation RF pulse for TOF MRA. a:** Shapes of real and imaginary parts of minimum phase RF pulse. **b:** Corresponding ramped excitation RF pulse profile. The profile is similar to the symmetric RF pulse in Figure 1.2, with the RF pulse center shifted to a later time point. 6
- 1.4 **Pulse sequence diagram for TOF MRA.** A minimum phase RF pulse and partial echo are used to keep the TE as short as possible. The magnetization transfer contrast (MTC) pulse and the presaturation pulse are applied in front of the slab excitation RF pulse. Flow compensation gradients are employed for slab-select and readout gradients. 7
- 1.5 **TOF MRA of a cat brain acquired at 9.4T.** Axial (a) and coronal (b) MIP images show detailed anatomy of cortical arteries and big veins. 8
- 1.6 **A scheme for converting phase image to phase-mask filter (negative phase-mask scheme).** Negative phase values from 0° and -180° are linearly mapped to mask values from 1 to 0. Positive phase values are all mapped to 1. 9
- 1.7 **BOLD MRV of a human brain acquired at 3T MR scanner.** (a) original magnitude and (b) phase images, (c) phase image after highpass filtering, (d) enhanced MRV magnitude image corresponding to image a multiplied by a phase-mask filter (generated from c), and (e) minimum-intensity projection of image d plus neighboring images over 10-mm thickness. Images in a–d and the center slice of e are at the same position. . . 11
- 2.1 **Dependence of image quality and signal to noise ratio (SNR) on TE with 9.4-T BOLD 3D microscopy (fraction of inspired oxygen = 30%). a and b:** Images of one

representative animal with TE = 10 ms (**a**) and 20 ms (**b**) after minimum-intensity projection of 1-mm thick coronal slabs from the 3D datasets (systemic arterial oxygen saturation level = 99%). CC = corpus callosum; IC = internal capsule. **c** and **d**: SNR values plotted as a function of TE for all studies ($N = 6$), where each line represents data from an individual animal; filled triangles represent data from **a** and **b**. Image insets are single-pixel thick (59 μm) coronal reconstructions (TE = 20 ms) from one study, where the signal spatial extent considered for each measurement is illustrated in two dimensions by the squares. The actual volumes for the signal measurement are $7 \times 7 \times 7 \text{ mm}^3$ (**c**) and $1.2 \times 1.2 \times 0.059 \text{ mm}^3$ (**d**), and the volume for noise measurement is $1.2 \times 1.2 \times 1.2 \text{ mm}^3$ (not shown). SNR is statistically highest for both regions of signal measurement when TE = 20 ms; * $p < 0.05$ 24

2.2 Oxygenation-dependent 9.4-T BOLD 3D microscopy study. Data were acquired with TE = 20 ms in an animal different from Figure 2.1a and b ($N = 6$ total). Displays are minimum-intensity projections of 1-mm thick coronal slabs. SaO₂ and FiO₂ in **a–c** represent values for the oxygen saturation level of systemic arterial blood and the fraction of inspired oxygen, respectively. Note that SaO₂ was calculated with the half saturation partial pressure of oxygen appropriate for rat hemoglobin. Regions within the rectangles (left) are expanded (right), with intensity and contrast levels adjusted to emphasize the SaO₂ dependence of vessels presumed to be arteries. Arterial candidates are marked when they are visible (arrows) and not yet visible (arrowheads). An arterial candidate from within the rectangular region in **c** are better visualized in expanded views of five consecutive single-pixel thick (59- μm) planes, where the long arrow indicates a vessel with increased contrast at deeper cortical regions. 26

2.3 Endogenous BOLD-contrast venograms at 9.4 T demonstrating various 2D reconstructions from one 3D dataset. Data were acquired with TE = 20 ms and the fraction of inspired oxygen = 30% (systemic arterial oxygen saturation level = 90%) from the same animal shown in Figure 2.2. Image reconstructions from single-pixel thick (59 μm) sections are shown along coronal (**a**), axial (**b**), and sagittal (**c**) directions. Minimum-intensity projections of 1-mm thick slabs are shown along coronal (**d**) and axial (**e**) directions, where projection slabs were centered at the planes of **a** and **b**, respectively. Images **a** and **d** are centered ~0.5 mm posterior to the reconstruction of Figure 2.2a. Green arrows in **d** and **e** indicate intracortical vessels that have visible branches. For a reconstruction from the dorsal cortical surface (**f**), pixels across a slab thickness of 1 mm were averaged. Colored ticks represent slice or slab centers for reconstructions with borders of the same color. The same intracortical vein (marked by small red circles) is seen in a coronal view (**a**) and as it drains to the cortical surface (**f**). A = anterior; D = dorsal; R = right; Amy = amygdala; Aq = aqueduct; CC = corpus callosum; Cor = cortex; D3V = dorsal third ventricle; GCC = genu corpus callosum; Hip = hippocampus; IC = internal capsule; SCC = splenium corpus callosum; Tha = thalamus; 3V = third ventricle. 28

2.4 Reconstructions from a 9.4-T BOLD 3D venographic dataset and cortical depth-dependent quantification of venous distributions. Data were acquired with

TE = 20 ms, and with the fraction of inspired oxygen = 30%. **a–g**: Data from one representative animal (different from Figures 2.1–2.3) (systemic arterial oxygen saturation level = 95%). **a**: Coronal view reconstructed by averaging pixels across a 1-mm thick slab. Red curves are 1.8 mm in length and indicate cortical depths of 0.1, 0.4, 1.0, and 1.6 mm, within the somatosensory cortex. **b**: A single-pixel thick (59- μm) reconstruction at the location of the yellow curve in **a** (cortical depth of 1.0 mm). The red square in **b** represents a $1.8 \times 1.8 \text{ mm}^2$ region within the somatosensory cortex. **c–f**: Expanded views of selected $1.8 \times 1.8 \times 0.059 \text{ mm}^3$ regions at 0.1 (**c**), 0.4 (**d**), 1.0 (**e**), and 1.6 mm (**f**) from the cortical surface, as indicated by the red curves in **a**. The green ticks in **b–f** represent the slab center of **a**. **g**: Histogram of the $1.8 \times 1.8 \times 0.059 \text{ mm}^3$ region at a cortical depth of 0.4 mm (shown in **d**) and its Gaussian curve fitting. Thirty discrete intensity bins were chosen based on minimum and maximum signal intensities within the region of interest. Venous pixel candidates (blue shading) are assigned as those with the intensity threshold = 85% of average tissue signal intensity (blue arrow). **h–j**: Cumulative intracortical venous densities vs. venous “size” (expressed as minimum in-plane contiguous pixels defining each identifiable venous vessel) at cortical depths of 0.4 (**h**), 1.0 (**i**), and 1.6 mm (**j**), for all studies (12 hemispheres). The right-most bar in each plot represents total venous density, which decreases with cortical depth ($p < 0.05$). Note the independent adjustment of vertical scales for better visualization. Measurements were performed within $1.4 \times 1.4 \times 0.059 \text{ mm}^3$ regions concentric with the $1.8 \times 1.8 \times 0.059 \text{ mm}^3$ regions illustrated in **d–f**, using default criteria for venous vessel identification (intensity threshold of 85% of average tissue signal intensity and depth contiguity of 4 pixels). The measurement error in cortical depth due to spatial variation of the cortical surface is $\sim 0.1 \text{ mm}$ ($N = 6$). 31

2.5 Images from a 3D *in vivo* two-photon angiographic dataset and cortical depth-dependent quantification of venous distributions. **a–c**: Data from one animal. The ability of this *in vivo* technique to resolve intracortical arteries and veins with much finer detail than by BOLD venography is illustrated in the maximum-intensity projected reconstruction ($0.456 \times 0.456 \times 0.6 \text{ mm}^3$) along the axial direction (**a**), where complete vascular networks including capillaries with $\sim 5\text{-}\mu\text{m}$ diameter are observed. Two-dimensional single plane images ($0.456 \times 0.456 \text{ mm}^2$) parallel to the surface at cortical depths of 0.1 mm (**b**) and 0.4 mm (**c**) show that relatively large sized vessels perpendicular to the cortical surface appeared as round shapes. Intracortical veins (and also arteries) can be traced between the surface and deep cortical regions, as seen in examples indicated by arrows. Note that these two-photon microscopy images (**b** and **c**) represent only $\sim 1/16$ the area as compared to the MRI venograms of Figures 2.4c–f. Cumulative intracortical venous densities (expressed as minimum venous diameter) are plotted as a function of diameter at cortical depths of 0.1 (**d**) and 0.4 mm (**e**) for all studies ($N = 5$). The right-most bar in each plot represents total venous density, which decreases with cortical depth ($p < 0.05$). Vertical scales were independently adjusted for better visualization. The density of smaller-diameter venous vessels (10–30 μm) is higher than that of larger-diameter vessels at both cortical depths. Density at 0.4-mm depth for intracortical venous vessels with diameter $\geq 15 \mu\text{m}$ is $5.3 \pm 1.8 / \text{mm}^2$, which roughly

corresponds to the venous density measurement of $5.7 \pm 1.0 / \text{mm}^2$ from our MRI data at the same depth using the default criteria (broken line). Note that due to a small field of view of two-photon microscopy, the two-photon densities were quantified for regions covering roughly half the area as compared to MRI data. 33

3.1 **Excitation RF pulse shape and profile used in TOF MRA and BOLD MRV.** **a:** Shapes of real and imaginary parts of the minimum phase RF pulse with ramped excitation profile. **b:** Two different excitation RF pulse profiles. One RF pulse, consisting of both the real and imaginary parts of the RF pulse with the flip angle of 25° , was used for TOF MRA (both single- and dual-echo acquisitions). The other RF pulse, consisting of only the real part of the RF pulse with the flip angle of 15° , was used for BOLD MRV (again both single- and dual-echo acquisitions). 42

3.2 **Pulse sequence diagram for CODEA.** The diagram is for the acquisition of K-space center regions of the first echo, without including spoiler gradients for simplicity. A minimum phase RF pulse was used to keep the TE of the first echo as short as possible. According to our echo-specific K-space reordering scheme, the 1st and 2nd phase-encoding gradients in the second echo were designed and applied independently from those in the first echo, i.e., rewound and applied again in the middle. Partial and full echoes were acquired for the first and second echoes, respectively. The magnetization transfer contrast (MTC) pulse was applied instead of the presaturation pulse only in one of the 3D datasets per subject. In the K-space center region in the second echo, only the real part of the excitation pulse was applied with no spatial presaturation pulse and no MTC pulse. The 1st phase-encoding loop was located outside the 2nd phase-encoding loop to minimize perturbations in the steady state condition, where N_1 and N_2 represent the total number of 1st and 2nd phase-encoding lines, respectively. 44

3.3 **K-space distribution of CODEA.** **a and b:** Cross sections of K-spaces at the center along the 2nd phase-encoding direction for the first (**a**) and the second (**b**) echoes. The K-space acquisition order was modified from the conventional, linearly-increasing order along the 1st phase-encoding direction. The initial $\frac{1}{4}$ of the total phase-encoding lines for the first echo were acquired at the end and the last $\frac{1}{4}$ of the total phase-encoding lines for the second echo were acquired at the beginning, as shown in **a** and **b**. **c:** RF pulses used for acquisition of each K-space region. When the K-space center region in the first echo was acquired (TOF-weighted MRA region), the excitation pulse with a spatially-varying ramp profile and a higher flip angle (20° – 30°) and the spatial presaturation pulse (or the MTC pulse if specified) were applied to enhance the arterial contrast in the first echo. When the K-space center region in the second echo was acquired (BOLD-weighted MRV region), the excitation pulse with a flat profile and flip angle of 15° was applied with no preparation pulse to improve the venous contrast in the second echo. Partial-echo and full-echo acquisitions were applied for the first and second echoes, respectively, as shown in **a** and **b**. 45

3.4 **Comparison of TOF angiograms acquired using the conventional single-echo and the CODEA methods.** **a–c:** The conventional single-echo TOF angiograms at MIP along

axial (**a**), sagittal (**b**), and coronal (**c**) directions over the entire 3D volume. **d–f**: The (first-echo) CODEA TOF angiograms at MIP along axial (**d**), sagittal (**e**), and coronal (**f**) directions again over the entire 3D volume. Scan resolution for all the angiograms is $0.43 \times 0.86 \times 1.4$ (mm³). Overall, the conventional single-echo and CODEA MRAs were comparable in image quality. The arrows in **b** and **e** identify a small downstream artery with a reduced vascular contrast in the CODEA MRA. 51

3.5 Comparison of BOLD venograms acquired using the conventional single-echo and the CODEA methods for the same subject as Figure 3.4. **a–c**: The conventional single-echo BOLD venogram at three different locations. **d–f**: The (second-echo) CODEA BOLD venogram at the same locations as **a–c**. The scan resolution for all the angiograms is $0.43 \times 0.86 \times 1.4$ (mm³). All images are minimum-intensity projections over a slab with 10-mm thickness. The conventional single-echo and CODEA MRVs were equivalent in image quality. 52

3.6 Comparison of multi-slab CODEA MRA/MRV and multi-slab dual-echo MRA/MRV without K-space reordering scheme in the same subject as Figures 3.4 and 3.5. **a** and **b**: TOF angiogram (**a**) and BOLD venogram (**b**) acquired using the CODEA with the echo-specific K-space reordering scheme. **c** and **d**: TOF angiogram (**c**) and BOLD venogram (**d**) acquired using the dual-echo angiography without K-space reordering (i.e., the conventional linearly-increasing k-space ordering was used in both echoes). An RF pulse with a flat excitation (flip angle 20°) was applied with no preparation pulse for the entire K-space regions in both echoes in **c** and **d**. Images in **a** and **c** are maximum-intensity projections over the entire 3D volume and images in **b** and **d** are minimum-intensity projections over a slab with 17-mm thickness. Scan resolution for all the angiograms is $0.43 \times 0.86 \times 1.4$ (mm³). Because a flat excitation pulse was applied for both echoes in **c** and **d**, the venous signals were relatively uniform (arrows in **d**). On the other hand, discontinuities were apparent in the arterial signals around the overlapping regions of the slab (arrows in **c**), which can be ascribed to the downstream blood saturation effects. Uniform vascular contrast with no discontinuity was observed in the MRA and MRV in the multi-slab CODEA acquisition (arrows in **a** and **b**). The arrowhead in **c** indicates signals from a large vein. 54

3.7 Comparison of CODEA MRA/MRV without and with the MTC pulse in a subject different from Figures 3.4–3.6. **a** and **b**: TOF angiogram (**a**) and BOLD venogram (**b**) acquired using the CODEA without the MTC pulse. **c** and **d**: TOF angiogram (**c**) and BOLD venogram (**d**) acquired using the CODEA with the MTC pulse. Images in **a** and **c** are maximum-intensity projections over the entire 3D volume, while images in **b** and **d** are minimum-intensity projections over a slab with 10-mm thickness. The MTC pulse improved the visualization of small vessels in TOF angiograms (arrows in **c**), with no apparent effect on the BOLD venogram (**d**). 56

4.1 Comparison of high-resolution BOLD fMRI map (a) and BOLD microscopic data (b). Activation foci in the somatosensory cortex (**a**) are correlated with intracortical veins (**b**), as indicated by arrows, and some activation foci outside the somatosensory cortex

(arrowheads) are located around regions of large draining veins including the superior sagittal sinus vein.	63
4.2 A representative CODEA MRA in a stroke patient. a: Maximum-intensity projection image along axial direction overall entire brain region. b and c: Maximum-intensity projection images along sagittal (b) and coronal (c) directions for a brain region excluding the fatty tissue region.	67
4.3 A representative CODEA MRV from the same subject as Figure 4.2. a-f: Minimum-intensity projection images at different locations over a thickness of 10 mm. The arrow in e represents a hypointense structure not detectable in the contralateral normal region. The arrowhead in f represents a site presumed to be infarction.	68
5.1 Two compartment model of a vein and surrounding tissue. Please see the text for details.	76

1.0 INTRODUCTION

1.1 REVIEW OF TOF MR ANGIOGRAPHY AND BOLD MR VENOGRAPHY

Depiction of vascular structures is required in a number of clinical diagnostic applications and basic research studies of vascular anatomy and physiology. Various magnetic resonance angiography (MRA) techniques are available. They are based on either the injection of exogenous contrast agents [gadolinium contrast-enhanced (CE) MRA] or the intrinsic property of blood [blood movement: time-of-flight (TOF) and phase-contrast MRA, susceptibility effects of deoxyhemoglobin: blood-oxygenation-level-dependent (BOLD) MR venography (MRV)]. Although CE-MRA is highly efficient and yields high-resolution vascular structures compared to unenhanced MRA techniques, it requires the injection of gadolinium contrast medium which is invasive and has been linked with causes of nephrogenic systemic fibrosis in patients with impaired renal function (1). In comparison, unenhanced MRA is non-invasive, does not require injection of contrast medium, and can be acquired repeatedly. The drawbacks of the unenhanced MRA include that it is technically more demanding and takes longer to acquire. Some of technical challenges involved in unenhanced MRA have been overcome with recent advances in MR hardware and software.

Among unenhanced MRA techniques, TOF MRA is the most commonly used in clinical practice. It is reliable and yields MRA with a good vascular contrast with a reasonable scan time (5–15 minutes) for the whole brain imaging. Phase-contrast MR angiography is another unenhanced MRA technique. It is mainly used for quantification of blood flow and rarely for imaging vascular structures because it is of limited spatial resolution and takes a long scan time (2,3).

Without use of gadolinium contrast medium, MRV can be obtained on the basis of BOLD contrast (4,5); that is, paramagnetic deoxyhemoglobin serves as an intrinsic venous blood contrast agent. Recent technical improvement such as phase-mask filtering allowed us to readily acquire BOLD MRV using standard clinical MR scanners (6,7). Clinical imaging of both TOF MRA and BOLD MRV are often desirable, because they complement the depiction of vascular pathologies. Nevertheless, MRV is usually not acquired to minimize the image acquisition time. It will be highly beneficial if we can acquire MRV while imaging MRA without increasing scan time. BOLD MRV technique is also a useful experimental tool for the investigation of hemodynamic processes associated with BOLD functional MRI. Thus, the objective of our study was to develop and assess BOLD MRV techniques for both experimental and clinical applications.

1.1.1 TOF MR Angiography

The basic principle of TOF MRA is that, when gradient-echo imaging with a short repetition time and relatively high flip angle is applied, MR signal intensity from the background tissues is suppressed while that from the fast-moving blood remains relatively unsaturated and enhanced (8). However, MR signal intensity of the flowing blood may not be uniform throughout its path and is spatially dependent. A fresh blood entering the imaging slab (upstream) would experience

increased number of RF excitations and become more saturated and less enhanced as it flows to the opposite side of the slab (downstream) (Figure 1.1). The maximum number (n) of RF excitations that blood encounters while flowing through an imaging slab can be expressed:

$$n = thk/(v*TR) \quad (1)$$

where TR , v , and thk , are repetition time, velocity of the blood, and thickness of the imaging slab, respectively. With increased n , the blood signal intensity saturates more. Thus, n should be minimized in order to preserve the initial inflow or TOF effect (i.e., MR signal intensity of the blood relative to the background tissue) (Figure 1.1). Evident from the Equation (1), n is reduced in the setting of thin slab, high blood velocity, and long TR . The velocity of blood is determined by physiology and is independent of imaging. While a thinner slab is preferred for preserving the inflow signal enhancement, it results in a lower signal to noise ratio (SNR) as a trade-off. TR is usually determined in consideration of the total scan time and spatial resolution.

The spatially dependent saturation in MR signal intensity of flowing blood is negligible in 2D TOF MRA, because of thin imaging slice and the acquisition of MRA sequentially one slice at a time. On the other hand, a flowing blood in 3D TOF MRA may experience a high degree of saturation because of thick imaging slab and undergoing increased number of RF excitations. The spatially dependent saturation effect of blood signals can be compensated and reversed by the application of an excitation RF pulse with a spatially-varying ramp profile (TONE: tilted optimized nonsaturating excitation (9,10)) (Figure 1.2).

While conventional RF pulse consists of only a real part (darker gray line in Figure 1.2a) and generates a flat excitation profile, a RF pulse with a ramped excitation profile is composed of both real and imaginary parts (darker and lighter gray lines in Figure 1.2a). The intensity and polarity of the RF imaginary part (lighter gray line in Figure 1.2a) determines the ramp slope and direction (Figure 1.2b), respectively. The ramped RF pulse was configured according to the Shinnar-Le Roux (SLR) algorithm (11) and the excitation profile was calculated with an embedded Runge-Kutta numerical solution of Bloch equations (Appendix A).

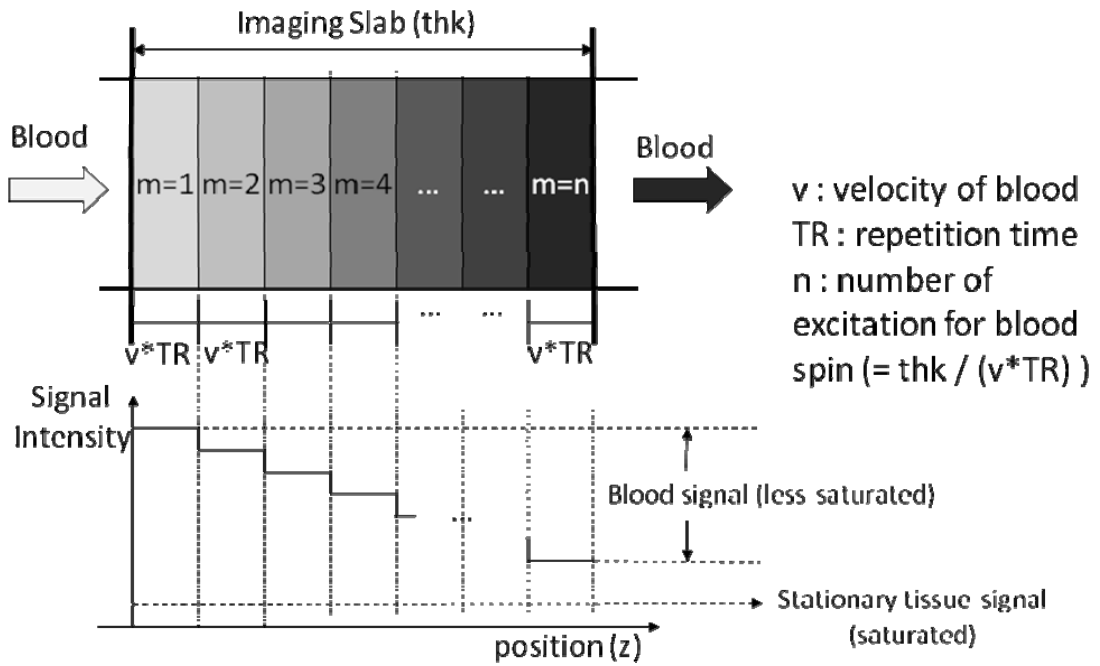


Figure 1.1 A schematic diagram illustrating the time-of-flight effect on MR signal intensities of moving blood and stationary tissue. MR signal intensity of a fresh blood is unsaturated and higher than that of the saturated stationary tissue. However, after entering the imaging slab, blood spins experience increased number of RF excitations and lose signal intensity, as they flow to the opposite side of the slab.

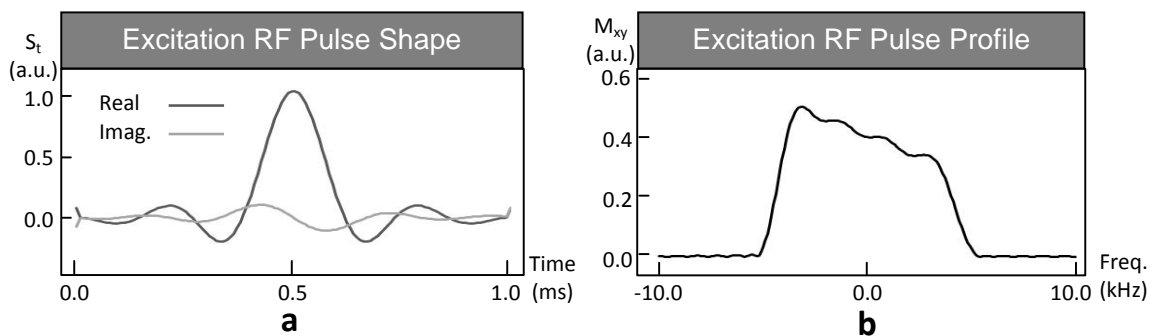


Figure 1.2 **Shape and profile of RF pulse for TOF MRA.** **a:** Shapes of real and imaginary parts of symmetric RF pulse. **b:** Corresponding ramped excitation RF pulse profile. The flip angle ranges from 20° to 30° .

With increase in imaging slab thickness, the SNR increases but MR signal intensity of the flowing blood undergoes a greater saturation. Therefore, 2D MRA with a thin slice (≤ 3 mm) is preferred for the preservation of the inflow effect while 3D MRA with a thick slab (≥ 20 mm) is favored for the SNR. When 3D MRA is acquired with doubling slab thickness, the scan takes twice long to maintain the same spatial resolution. The SNR improves by $\sqrt{2}$. Essentially the same effect can be achieved by doubling the number of averages or 100% oversampling along phase- or slice-encoding directions (12). A technique that combines the strengths of both 2D TOF (low MR inflow signal saturation) and 3D TOF (high SNR) MRA is multiple overlapping thin slab acquisition (MOTSA) technique (13). In this technique, multiple overlapping 3D TOF slabs (~ 20 mm) are acquired similar to multiple 2D TOF slices but to cover a large volume (typically ≥ 60 mm). Partial overlapping of neighboring slabs reduces the saturation effect in continuous blood vessels. When the MOTSA is used with an appropriate ramped RF pulse, blood vessels traversing over multiple slabs can maintain continuous signal intensities between slabs. Visualization of small blood vessels on 3D MRA improves with the use of MOTSA, compared to the single-slab acquisition (13).

The image quality of TOF MR angiography can be also improved by use of two additional RF pulses of a magnetization transfer contrast (MTC) pulse and a spatial presaturation pulse. The MTC pulse selectively suppresses the background tissue signals without affecting the blood signals, thereby enhancing tissue contrast between the hyperintense blood vessel and dark background tissue (14,15). The MTC pulse is applied prior to the excitation RF pulse at an off-resonant frequency (usually about 1500 Hz off from the resonance frequency at clinical field strengths). The spatial presaturation pulse applied in the position next to the imaging slab on the side of venous blood return suppresses venous signals while accentuating hyperintense arterial signals.

Flow compensation and short echo time (TE) minimize flow-related dephasing effects in TOF angiography. Since higher order flow compensations increase TE, only the *first-order* flow

compensation is typically applied. In the same reason, the flow compensation is commonly applied for the *slab select* and *readout* gradients not for the phase encoding gradients (15,16). This is because, while the center of k-space in the phase encoding governs the vascular contrast and signal, flow compensation for the center is not as effective as that for the periphery of the k-space given low phase encoding gradients in the center of the k-space. TE can be reduced by the application of different strategies. First, the conventional symmetric excitation RF pulse is replaced with a minimum-phase RF pulse (Figure 1.3a). Second, the readout dephasing gradient strength is reduced by having the echo center formed at an earlier time point and partially discarding initial high-frequency data points (partial-echo acquisition, Figure 1.4). Note that an asymmetric RF pulse (Figure 1.3a) can be configured according to the Shinnar-Le Roux algorithm, thereby minimizing the ringing in the excitation profile (Figure 1.3b).

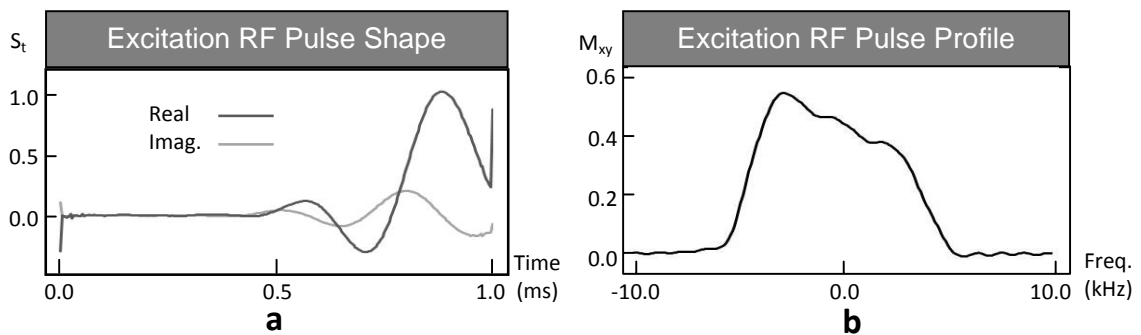


Figure 1.3 Shape and profile of Minimum-phase Shinnar-Le Roux excitation RF pulse for TOF MRA. a: Shapes of real and imaginary parts of minimum phase RF pulse. **b:** Corresponding ramped excitation RF pulse profile. The profile is similar to the symmetric RF pulse in Figure 1.2, with the RF pulse center shifted to a later time point.

A typical pulse sequence diagram for 3D TOF MRA is shown in Figure 1.4. The diagram demonstrates implementation of all aforementioned techniques, except for the MOTSA that cannot be described in this pulse sequence diagram.

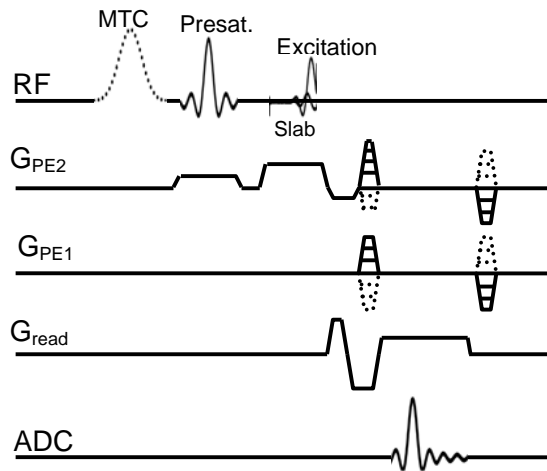


Figure 1.4 **Pulse sequence diagram for TOF MRA.** A minimum phase RF pulse and partial echo are used to keep the TE as short as possible. The magnetization transfer contrast (MTC) pulse and the presaturation pulse are applied in front of the slab excitation RF pulse. Flow compensation gradients are employed for slab-select and readout gradients.

Finally, the quality of TOF angiogram can be improved with zero-filled interpolation during the image reconstruction (17). Zero-filled interpolation reduces partial volume averaging effects. TOF MRA is commonly displayed with maximum-intensity projection (MIP). An example TOF MRA of an *in vivo* cat brain is shown in Figure 1.5. This was acquired at 9.4T with a home-made two-ring type quadrature surface RF coil (inner diameter = 2.2 cm). Scan parameters were TR 50 ms, TE 3.6 ms, field of view (FOV) $40 \times 20 \times 20$ (mm³), Matrix $384 \times 192 \times 192$, nominal flip angle 20°, MTC pulse, no spatial presaturation pulse, and total scan time ~35 min. The acquired data were zero filled to an matrix size of $512 \times 256 \times 256$, before the application of Fourier transform. Detailed anatomy of cortical arteries and big veins including the superior sagittal sinus vein are depicted in the MRA.

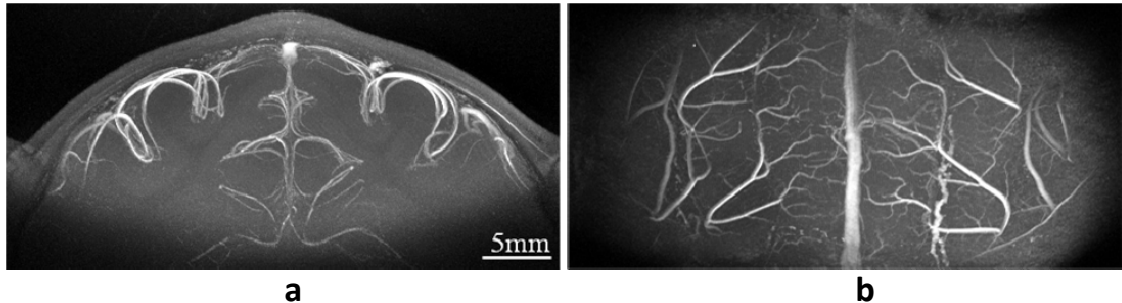


Figure 1.5 TOF MRA of a cat brain acquired at 9.4T. Axial (a) and coronal (b) MIP images show detailed anatomy of cortical arteries and big veins.

1.1.2 BOLD MR Venography

The first non-invasive demonstration of BOLD MR venogram (MRV) was performed on animal brains at high fields (7 and 8.4T) (4,5). In these studies, hypointense venous signals in mouse brains were detected and modulated by changing oxygen concentrations in inhaled gas. The venous signal contrast depends on the oxygenation level of venous blood (i.e., susceptibility effect of deoxyhemoglobin). At a high magnetic field ($\geq 7T$), T_2^* of venous blood is much shorter than T_2^* of tissue. As a result, venous blood signal can be readily differentiated from background tissue signal and detected in MR imaging with TE sufficiently longer than T_2^* of venous blood. Furthermore, with increased TE, the susceptibility effect extends to a greater distance in the surrounding tissue (4,5), hence veins would show apparent increase in size and prominence.

The detailed mathematical basis of BOLD contrast in a venous vessel is described in Appendix B. In brief, deoxyhemoglobin in venous blood increases magnetic susceptibility and causes spatially varying phase shift in complex signals. Since MR signal of a pixel corresponds to the integration of all the spins within the pixel, the magnitude of the pixel signal is reduced with

increased degree of heterogeneous phase shift within the pixel. At ultra high fields, combined phase shift effect and short T_2^* of venous blood accentuates contrast between the vein and background on the magnitude image.

At the conventional clinical field strength of 1.5T, venous blood and tissue have similar T_2^* values. This leads to a reduced susceptibility effect and venous contrast against the background tissue on the magnitude image. However, the venous contrast can be markedly improved with the use of a long TE (allowing a -180° intravascular phase shift relative to the stationary tissue) and a phase-mask filtering applied to the original magnitude images (7,18). High-pass filtering of phase images is necessary for phase-mask filtering to remove low-frequency phase shifts induced by background magnetic field inhomogeneity (19). A mask image is generated from the high-pass filtered phase image by mapping negative phase value of 0° and -180° onto 1 and 0, respectively, and linearly scaling the values between them. Positive phase values are all mapped to 1 (Figure 1.6). This mask scheme (negative phase mask scheme) is reported to be highly effective for venous contrast enhancement compared to other schemes (20). At a clinical magnetic field MR scanner, BOLD MRV is usually generated by multiplying the negative phase mask four times to the magnitude image (6).

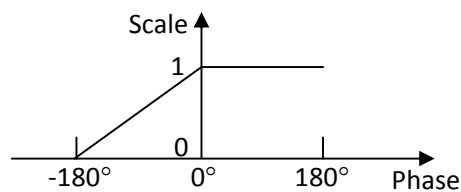


Figure 1.6 **A scheme for converting phase image to phase-mask filter (negative phase-mask scheme).** Negative phase values from 0° and -180° are linearly mapped to mask values from 1 to 0. Positive phase values are all mapped to 1.

The phase-mask filtering technique is most effective at the phase difference of 180° between the background tissue and intravascular venous blood in T_2^* -weighted images (7,18). Phase difference is a complex process associated with multiple factors including venous oxygenation level, angle between vessel orientation and main magnetic field, magnetic field strength, TE, and partial volume effects. In a two compartment model of vein and surrounding tissue, intravascular phase shift is expressed as

$$\Delta\phi = -\gamma \cdot 2 \cdot \pi \cdot \Delta\chi_0 \cdot Hct \cdot (1 - Y) \cdot \left(\cos^2(\theta) - \frac{1}{3}\right) \cdot B_0 \cdot TE \quad (2)$$

where γ is gyromagnetic ratio of protons (2.68×10^5 rad/s/mT), $\Delta\chi_0$ is susceptibility difference between fully oxygenated and deoxygenated red blood cells (0.18×10^{-6} in CGS unit (21)), Hct is hemotocrit level, Y is blood oxygenation level, θ is an angle between the vein of interest and the main magnetic field, and B_0 is the main magnetic field. Regarding the data acquisition, the selection of TE is the most important factor. At $Hct = 0.45$, $Y = 0.54$, and $\theta = 0$, the optimal TE for phase-mask filtering is approximately 50 ms and 25 ms at magnetic field strengths of 1.5T and 3T, respectively. These relatively long TE values dictate the determination of other scan parameters.

A BOLD MRV dataset acquired at 3T is shown in Figure 1.7. Scan parameters were TR 40 ms, TE 20 ms, field of view (FOV) $240 \times 180 \times 80$ (mm³), matrix $512 \times 192 \times 64$, flip angle 15° , and total scan time 9.8 min. The acquired data were zero filled to matrix size of $512 \times 384 \times 170$, before the application of Fourier transform. Venous contrast is weakly visible in the original magnitude (Figure 1.7a). While anatomical structures are not discernible in the original phase image (Figure 1.7b), they become more visible after a high-pass filtering process removing phase signals associated with background field inhomogeneity (Figure 1.7c). The filtered phase image is converted to a negative phase mask using the algorithm described in Figure 1.6. The enhanced MRV is generated from the original magnitude image multiplied four times by the negative phase mask (Figure 1.7d). Minimum intensity projection image is obtained

by projecting the enhanced MRV over a slab (10-mm thickness in Figure 1.7e). Detailed venous vasculature is depicted.

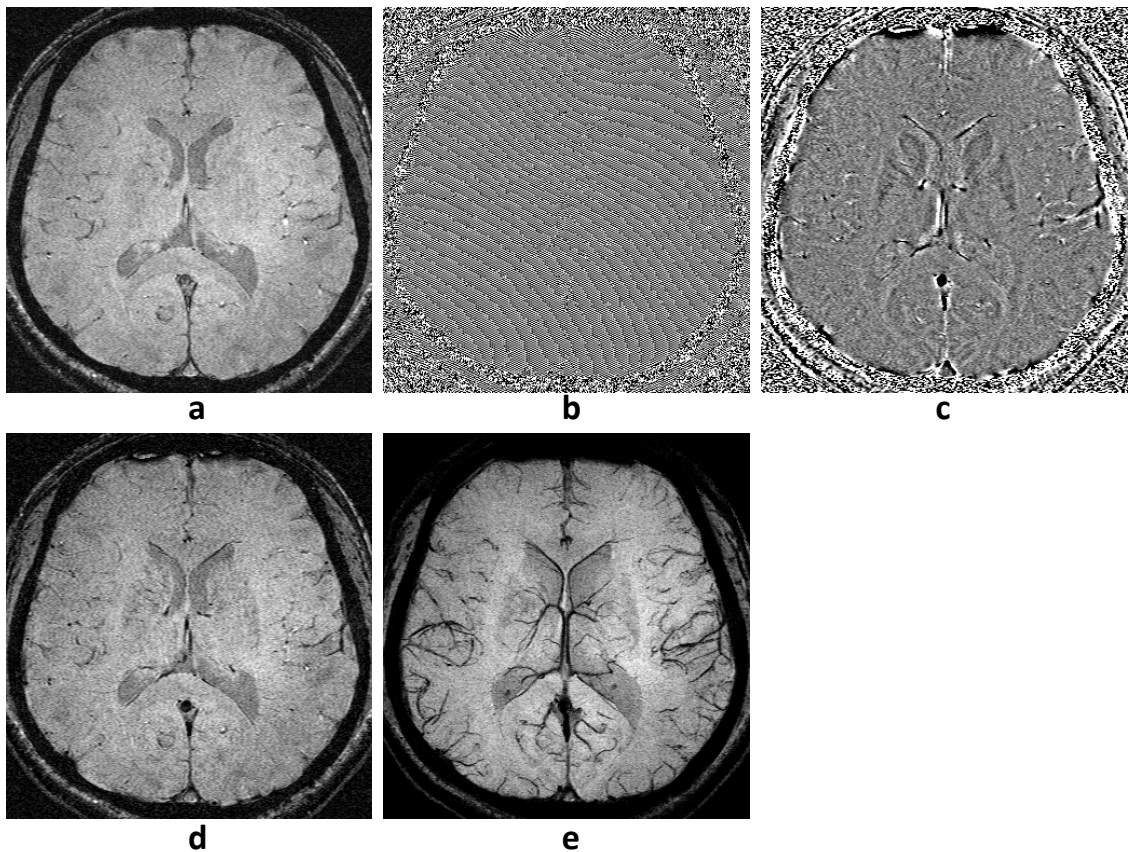


Figure 1.7 **BOLD MRV of a human brain acquired at 3T MR scanner.** (a) original magnitude and (b) phase images, (c) phase image after highpass filtering, (d) enhanced MRV magnitude image corresponding to image a multiplied by a phase-mask filter (generated from c), and (e) minimum-intensity projection of image d plus neighboring images over 10-mm thickness. Images in a–d and the center slice of e are at the same position.

1.2 STATEMENT OF PROBLEM

BOLD techniques have been used in a vast range of applications including functional MRI (fMRI) and clinical MR venography (MRV) of brain vasculature. Despite the immense success of BOLD fMRI applications, our understanding of complex neuronal and hemodynamic processes associated with BOLD techniques is limited. In BOLD MRV, a number of tissues and structures (e.g., bone, nerve, connective tissue, air, iron, blood clots) may present with hypointense MR signals similar to venous signals. Veins on BOLD MRV may appear larger than the actual size due to extravascular susceptibility effects of deoxyhemoglobin. An experimental investigation with BOLD MRV may allow us to expand our knowledge in hemodynamic process involved in BOLD fMRI. BOLD techniques are also clinically useful. In clinical brain imaging studies, imaging both time-of-flight (TOF) MR angiogram (MRA) and BOLD MRV are often desirable, because they complement the depiction of vascular pathologies. Nevertheless, MRV is usually not acquired to minimize the image acquisition time. It will be highly beneficial if we can acquire MRV while imaging MRA without increasing scan time. Thus, the objective of our study was to develop and assess BOLD MRV techniques for both experimental and clinical applications.

For the experimental evaluation of BOLD MRV, our study focuses on the optimization of BOLD MR venography at 9.4T and the assessment of the venous origin of hypointense vasculature with modulation of oxygenation using a rat brain model. The relative T_2 values of venous blood versus brain parenchyma are considerably higher at ultra high fields: 5–7 ms versus 40 ms at 9.4T (22) while 60–100 ms versus 80–90 ms at 1.5T (23). We expect a similar trend in

the T_2^* values. Since no study on the optimization of BOLD MRV at ultra high fields was published in the literature, the optimal scan condition for our animal study needs to be determined.

For the clinical application of BOLD MRV, our study focuses on the development and assessment of an efficient clinical BOLD MRV technique. A recent study showed a simultaneous acquisition of TOF MRA and BOLD MRV using a dual-echo sequence at a single imaging session (24). The scan parameters used in this study, however, were not optimal for concurrent TOF MRA and BOLD MRV. The optimization of scan conditions satisfying both TOF MRA and BOLD MRV is difficult, because they require conflicting tissue signal characteristics: e.g., the background tissue signal should be suppressed in the TOF MRA, while it should be enhanced in the BOLD MRV. Thus, it is desirable to develop a new dual-echo imaging technique optimizing the conflicting scan conditions for TOF MRA and BOLD MRV.

In this dissertation, chapter II is dedicated to the optimization of BOLD MRV using a rat brain model at 9.4T, confirmation of BOLD venous origin, investigation of venous detectability, and extension to BOLD microscopy. Chapter III is focused on the development of a new compatible dual-echo arteriovenography (CODEA) technique for simultaneous acquisition of TOF MRA and BOLD MRV in a single acquisition without compromising the image quality at a 3T clinical MR scanner. As an application and extension of Chapter II, Chapter IV.A is dedicated to the comparison of BOLD microscopy and BOLD fMRI for investigation of spatial limitation of BOLD fMRI technique. Similarly, as an application and extension of Chapter III, Chapter IV.B is dedicated to the application of the CODEA technique to the imaging of patients with stroke.

2.0 IMAGING BRAIN VASCULATURE WITH BLOOD OXYGENATION LEVEL-DEPENDENT MICROSCOPY: MR DETECTION LIMITS DETERMINED BY IN VIVO TWO-PHOTON MICROSCOPY

2.1 INTRODUCTION

Venous blood oxygenation level dependent (BOLD) contrast – originally described by Ogawa et al. (4,5) – relies on the magnetic susceptibility of paramagnetic deoxyhemoglobin (dHb). This endogenous contrast is the most commonly-used mechanism in functional MRI (25-27); neural activity induces a blood oxygenation increase (dHb concentration decrease) in capillaries, before draining to intracortical venous vessels, and finally to large pial veins. Since BOLD fMRI signal magnitude is closely related to baseline venous blood volume and oxygenation level, larger veins, which can be far from the sites of neural activity, often have larger BOLD signal changes relative to smaller venules and capillaries (28-31). High-resolution vascular imaging (capable of detecting extremely small veins) gives investigators a tool to examine the relationship between fMRI signal and vascular structures.

The first non-invasive depiction of vascular patterns with the BOLD effect was demonstrated in magnitude T_2^* -weighted images of rat brain at high magnetic fields (4,5). But at the clinical field strength of 1.5 T, venous contrast in magnitude images is relatively poor, so venous contrast in the human brain has been enhanced by phase-contrast filtering to reveal detailed venous structure (7,18). When the phase difference between tissue and intravascular

venous blood in T_2^* -weighted images is 180° , this post-processing technique is most effective (7,18); however, the phase difference is a complicated function of several factors including venous oxygenation level, angle between vessel orientation and main magnetic field, magnetic field strength, and echo time (TE). Alternatively, at field strengths ≥ 7 T, simple magnitude T_2^* -weighted images without phase-contrast filtering clearly have shown some venous discrimination in animal and human brain (4,5,32,33). At 9.4 T, T_2 of venous blood is much shorter than T_2 of tissue or systemic arterial blood (22), and this trend is also expected for T_2^* values. Contrast between tissue and venous blood can therefore be enhanced in magnitude T_2^* -weighted images at high field by setting TE sufficiently long relative to T_2^* of venous blood. Additionally, longer TE values extend the susceptibility effect to greater distances in the surrounding tissue, causing the veins to appear larger (5,25), which increases their detectability.

In this paper, *in vivo* T_2^* -weighted BOLD microscopy was performed using a 3D gradient-echo pulse sequence to obtain 78- μm isotropic scan resolution in rat brains at 9.4 T. Both signal to noise ratio (SNR) of tissue and contrast to noise ratio (CNR) between tissue and veins were maximized by experimental optimization of TE, which was compared with theoretical expectations. The levels of inspired oxygen were changed to confirm that the hypointense pixels in T_2^* -weighted images were indeed of venous origin, and not magnetic susceptibility effects from sources other than venous dHb (e.g., arterial dHb, iron deposits, air/tissue/bone interfaces). Venous size-dependent density was quantified at selected cortical depths within the somatosensory area. Since intracortical venous diameters are not directly quantifiable by BOLD, the limits of detectability were determined by computer simulations and by density comparison with another imaging modality. Since vessel diameters measured by any histological techniques may differ from *in vivo* values and there are insufficient *in vivo* data, we determined diameter-dependent venous density in separate animals under similar *in vivo* conditions by 3D two-photon excitation laser scanning microscopy with intravenous injection of a fluorescent

marker – an invasive, but “gold-standard” technique that can provide cortical depth-resolved measurements for all vessels between the cortical surface and 0.6-mm depth (34).

2.2 METHODS

2.2.1 Animal preparation

Eleven male Sprague-Dawley rats weighing 260–450 g were used for MRI studies at the University of Pittsburgh ($N = 6$), and for two-photon microscopy studies at the National Institute of Radiological Sciences (Japan) ($N = 5$), with approval from the Institutional Animal Care and Use Committee (IACUC) at each respective institute. For all studies (MRI and two-photon), the rats were initially anesthetized by inhalation of 5.0% isoflurane in a 7:3 mixture of $N_2O:O_2$ or $N_2:O_2$, and then intubated for mechanical ventilation (RSP-1002, Kent Scientific, CT, USA and SAR-830AP, CWE, PA, USA). The isoflurane level was reduced to 2.0% for surgical preparation. The femoral artery and femoral vein were catheterized for blood gas sampling and for administration of fluid and/or fluorescent marker, respectively. Then the $N_2O:O_2$ mixture was replaced with an air: O_2 mixture in a ratio to attain a fraction of inspired oxygen (FiO_2) of 30% for MRI studies and 30-35% for two-photon studies, and the isoflurane level was adjusted to ~1.5% for MRI studies and ~1.3% for two-photon studies. These small differences in FiO_2 and isoflurane levels are unlikely to change physiological conditions and consequently vessel diameters. Rectal temperature was maintained at 37 ± 0.5 °C. Ventilation rate and volume were adjusted based on the blood gas analysis results (Stat profile pHox; Nova Biomedical, MA, USA and i-Stat, Fusoyakuhin, Japan) to maintain carbon dioxide partial pressure levels within 30–40 mm Hg. Oxygen saturation levels were calculated using Hill’s equation with rat hemoglobin half saturation partial pressure (P_{50}) of oxygen = 38 mm Hg (35), Hill

coefficient = 2.73, and measured partial oxygen pressure values. Note that the blood gas analyzers used human hemoglobin P_{50} of ~26 mm Hg for calculation of oxygen saturation levels. For MRI studies, the head of the animal was carefully secured to a home-built cradle by means of ear pieces and a bite bar. Reduced FiO_2 values of 21% and 15% were attained in oxygenation-dependent MRI studies by changing the gas mixture to air and air: N_2 mixtures, respectively. MR images were not acquired until at least 10 minutes after each target O_2 level was achieved.

For two-photon microscopy studies, the left skull was thinned ($5 \times 7 \text{ mm}^2$ area). *In vivo* cortical vasculature was imaged following a 0.2–0.4 ml intravenous bolus injection of 1- μ M quantum dots (Qdot[®] 605 ITK[™] Amino (PEG), Invitrogen, CA, USA), which remained in bloodstream and thus were used as a contrast agent for blood vessels.

2.2.2 MRI Studies

2.2.2.1 Data collection

All experiments were carried out on a Varian 9.4 T / 31-cm MRI system (Palo Alto, CA) with an actively-shielded gradient coil of 12-cm inner diameter, which operates at a maximum gradient strength of 400 mT/m and a rise time of 130 μ s. A home-built quadrature radiofrequency (RF) surface coil (inner diameter of each of 2 lobes = 1.6 cm) was positioned on top of the animal's head and provided RF excitation and reception. Localized shimming was performed with point resolved spectroscopy (36) over a volume ($\sim 15 \times 10 \times 10 \text{ mm}^3$) covering most of the brain to yield a water spectral linewidth of 30–50 Hz.

BOLD microscopy was performed with 3D RF-spoiled gradient-echo imaging. The pulse sequence similar to that presented by Reichenbach et al. (7), but flow compensation was performed on the readout and slab-select directions only. Slab selection (1.5 cm) is required in the

anterior-posterior direction, since the sensitive volume of the surface coil exceeds the volume of interest (VOI). Also the inclusion of small TE values in the TE-dependent studies requires the shortest possible time between RF peak amplitude and start of data collection (T_{delay}). Therefore a minimum-phase Shinnar-Le Roux excitation pulse (11) was applied in the presence of a gradient, allowing T_{delay} to be fixed at 5 ms for all studies. The RF power level was adjusted to maximize subcortical signal. Imaging parameters were: repetition time = 50 ms, field of view = $3.0 \times 1.5 \times 1.5 \text{ cm}^3$, corresponding matrix size = $384 \times 192 \times 192$, voxel resolution = $78 \mu\text{m}$ (isotropic), and number of averages = 2. The largest field of view was along the readout direction (lateral-medial). Partial Fourier sampling (75%) was applied in both phase-encode directions. Each 3D venographic dataset was acquired in 34.5 min. In TE-dependent studies, the longest possible readout time (T_{read}) (corresponding to the narrowest possible acquisition bandwidth) was chosen to minimize the noise, while maintaining the relationship of $\text{TE} = T_{\text{delay}} + T_{\text{read}}/2$; however T_{read} was always $\leq 40 \text{ ms}$ (i.e. $\text{TE} \leq 25 \text{ ms}$) to limit susceptibility artifacts. Consequently, datasets with TE values of 10, 13, 16, 20, and 24 ms, and corresponding T_{read} values of 10, 16, 22, 30, and 38 ms were acquired at $\text{FiO}_2 = 30\%$. For the study of oxygenation dependence, additional datasets at $\text{FiO}_2 = 21\%$ and 15% were acquired with $\text{TE} = 20 \text{ ms}$ ($T_{\text{read}} = 30 \text{ ms}$). Therefore, a total of seven 3D datasets were acquired for each animal; five TE-dependent datasets at $\text{FiO}_2 = 30\%$, and one each at $\text{FiO}_2 = 21$ and 15% .

2.2.2.2 General venographic reconstruction, display, and SNR determination

Each 3D dataset was first zero-filled to a matrix size of $512 \times 256 \times 256$ and then Fourier-transformed to yield datasets with nominal isotropic voxel dimensions of $59 \mu\text{m}$. All displays and quantifications of data are based on magnitude data only.

To generate 2D views from any of the 3D datasets, a single-pixel (59 μm) plane or a 17-pixel (1 mm) slab was selected along one of the three orthogonal directions. Vessel detection within slabs was improved by minimum-intensity projection (18) or by averaging pixels across the slab thickness.

Lastly – for all displays and quantification of data (unless noted otherwise), intensity variation due to the inhomogeneous RF field of the surface coil was reduced with a 2D non-uniformity correction algorithm (37) after all other processing was complete. Intensity and contrast levels of images appearing within each figure were independently adjusted.

SNR values were determined in TE-dependent datasets both from signal within large VOIs containing vessels ($7 \times 7 \times 7 \text{ mm}^3$) at the brain center, and from signal within small cortical regions without prominent vessels ($1.2 \times 1.2 \times 0.059 \text{ mm}^3$) selected from coronal views, while noise for both was measured from $1.2 \times 1.2 \times 1.2 \text{ mm}^3$ regions outside the brain. Rician distribution of intensity was accounted for by quantification as $\text{SNR} = \sqrt{M^2 - \sigma^2} / \sigma$, where M and σ represent measured signal (mean) and noise (standard deviation), respectively (38). Non-uniformity corrections were not applied when SNR was evaluated.

2.2.2.3 Reconstruction of flattened cortical planes

Cross-sectional views of vessels aligned perpendicular to the cortical surface were generated by performing cortical flattening along the lateral-medial dimension (minor anterior-posterior curvature was ignored). This procedure involved first manually defining a curve at a select cortical depth on a 59- μm thick coronal view containing the somatosensory area. At 59- μm intervals along this curve, pixel intensities were calculated by linear interpolation of the 4 nearest pixels to construct a flat line with 59- μm resolution, where distances along the line preserve the original distances along the curve. This entire process utilizing the same curve was

repeated for each 59- μm thick coronal view from the 3D dataset, and each of these lateral-medial lines were then stacked in the anterior-posterior direction to compose a 2D cross-sectional view at the selected cortical depth.

2.2.2.4 Depth-dependent quantification of venous parameters

Venous pixel candidates were chosen and “identifiable veins” were assigned as follows. After comparison of coronal views with a stereotaxic atlas (39) for coordinate assignment, bilateral rectangular columns oriented perpendicular to the cortical surface were defined within the 3D dataset such that their centers intersected the surface at 1.0 mm posterior and ± 2.6 mm lateral to bregma. A column length spanned the entire cortical depth, with flattened cross-sectional areas of $1.8 \times 1.8 \text{ mm}^2$. These columns incorporate as much somatosensory area as possible to reduce errors in venous quantification due to any potential tissue heterogeneity. Pixel intensities of each $1.8 \times 1.8 \times 0.059 \text{ mm}^3$ section of a column (59- μm isotropic resolution) were calculated as previously described for cortical flattening. A VOI was then constructed consisting of all $1.8 \times 1.8 \text{ mm}^2$ planes between cortical depths of 0.4 and 1.8 mm within the column; 2D planes with cortical depths < 0.4 mm were excluded due to extravascular signals from pial veins. Veins were identified within this VOI only if they passed criteria based on intensity threshold and depth contiguity. First, the intensity threshold for venous pixel candidates was determined by fitting a signal intensity histogram of each 2D plane within the VOI to a Gaussian curve, the center of which represents the average tissue signal intensity. Venous pixel candidates were assigned as those whose signal intensity did not exceed a threshold (default = 85%) based on the average tissue signal intensity. Venous pixel candidates below the intensity threshold were then tested for depth contiguity across each plane within the VOI. Since most intracortical veins are perpendicular and continuous to the cortical surface, an identifiable vein was assigned only if

venous pixel candidates were also connected over a minimum number of contiguous planes, which by default was 4 planes based on a compromise between detection of vessels (as short as $\sim 240 \mu\text{m}$) vs. false assignment due to noise.

The density of identifiable intracortical veins and the apparent spatial extent of their cross sections were examined in equidistant $1.8 \times 1.8 \times 0.059 \text{ mm}^3$ sections within the VOI, positioned 0.4, 1.0, and 1.6 mm from the cortical surface. For each of these sections, a binary map representing only the pixels that passed both criteria for identifiable veins was created. To minimize quantification problems associated with veins located at the edge of each plane, the measurements were performed only for veins whose minimum-intensity pixel was located within a smaller $1.4 \times 1.4 \times 0.059 \text{ mm}^3$ region concentric with the $1.8 \times 1.8 \times 0.059 \text{ mm}^3$ region (gap between edges of these two regions = 3 pixels). Intracortical venous density vs. apparent size was determined at the select cortical depths after separating identifiable veins based on their in-plane contiguous pixels in these binary maps. Pixel locations of the same identifiable veins were also located on the $1.8 \times 1.8 \times 0.059 \text{ mm}^3$ grayscale sections (linearly-interpolated and 2D RF non-uniformity corrected), from which full width at half-minimum intensity (FWHMin) values for the anterior-posterior and lateral-medial directions were averaged to yield one FWHMin value per vein.

2.2.3 Two-photon Microscopy Studies

For two-photon microscopy studies, the left skull was thinned ($5 \times 7 \text{ mm}^2$ area). *In vivo* cortical vasculature was imaged following a 0.2–0.4 ml intravenous bolus injection of 1- μM quantum dots (Qdot[®] 605 ITK[™] Amino (PEG), Invitrogen, CA, USA), which remained in bloodstream and thus were used as a contrast agent for blood vessels.

Intracortical vasculature was three-dimensionally imaged *in vivo* with laser scanning microscope (TCS SP5 MP, Leica Microsystems, Germany). Injected quantum dots were excited with a Ti:sapphire laser (MaiTai Hp1020, Spectra-physics, CA, USA) at 900-nm wavelength with ~2.0 W output, and emitted orange-fluorescent light (605 nm). An image with 512×512 matrix size and 0.89- μm in-plane and 10- μm depth resolutions ($0.456 \times 0.456 \text{ mm}^2$ field of view) was obtained with the $\times 20$ water-immersion objective lens (0.5 numerical aperture). Four adjacent images (2 by 2) were acquired by shifting the animal position relative to the microscope for coverage of a $0.91 \times 0.91 \text{ mm}^2$ region of the primary somatosensory cortex relatively void of large pial vessels, centered $1.0 \pm 0.4 \text{ mm}$ posterior and $2.6 \pm 0.5 \text{ mm}$ left of bregma. Vascular images were obtained from the cortical surface to a depth of ~0.6 mm, in 0.01-mm steps. Since pial arteries and veins were visually distinguished based on the differences in their color (artery is light vs. vein is dark red), intracortical venous network was identified by tracking from the pial vasculature. Intracortical venous density and cross-sectional diameter were measured within the four adjacent images ($0.91 \times 0.91 \times 0.01 \text{ mm}^3$) at cortical depths of 0.1 and 0.4 mm. For display purposes, images from contiguous planes were maximum-intensity projected.

2.3 RESULTS

2.3.1 MRI Studies

2.3.1.1 TE-dependent studies

Studies performed at $\text{FiO}_2 = 30\%$ with minimum acquisition bandwidths (10.1–38.4 kHz) show that the hypointense pixels become darker and more numerous as TE lengthens, due to increased susceptibility effects from dHb (Figure 2.1a and b). Contrast between gray and white matter also

improves at longer TE values, as can be seen by the darkening of the corpus callosum and internal capsule (Figure 2.1b). SNR values from $7 \times 7 \times 7 \text{ mm}^3$ VOIs in the center of the brain (Figure 1.1c) and from $1.2 \times 1.2 \times 0.059 \text{ mm}^3$ cortical regions without prominent vessels within coronal sections (Figure 2.1d) were measured as a function of TE ($N = 6$). For the five conditions tested, SNR was highest when TE = 20 ms ($T_{\text{read}} = 30$ ms) for both regions, which is statistically significant (Wilcoxon signed rank test, $p < 0.05$). An echo time of 20 ms is ~ 3 times longer than T_2 of venous blood, resulting in negligible intravascular venous blood signal; therefore CNR between tissue and veins should also be near optimal when TE = 20 ms. Thus, further studies were restricted to TE values of 20 ms.

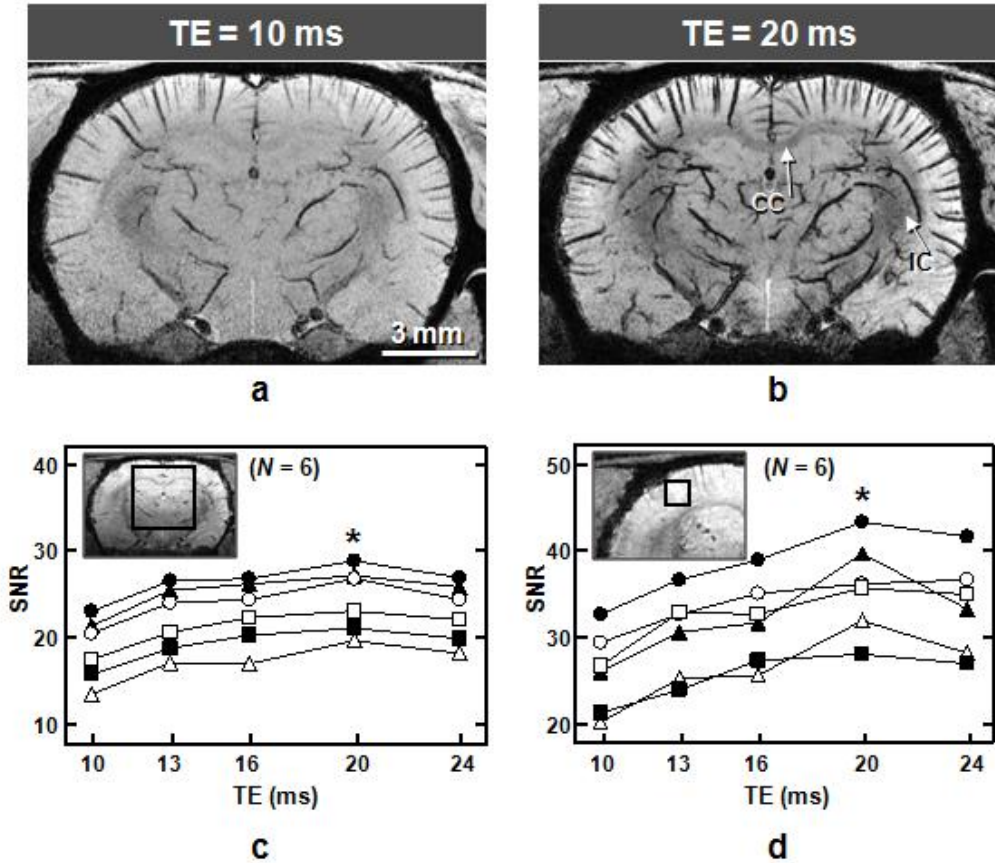


Figure 2.1 **Dependence of image quality and signal to noise ratio (SNR) on TE** with 9.4-T BOLD 3D microscopy (fraction of inspired oxygen = 30%). **a** and **b**: Images of one representative animal with TE = 10 ms (**a**) and 20 ms (**b**) after minimum-intensity projection of 1-mm thick coronal slabs from the 3D datasets (systemic arterial oxygen saturation level = 99%). CC = corpus callosum; IC = internal capsule. **c** and **d**: SNR values plotted as a function of TE for all studies ($N = 6$), where each line represents data from an individual animal; filled triangles represent data from **a** and **b**. Image insets are single-pixel thick ($59 \mu\text{m}$) coronal reconstructions (TE = 20 ms) from one study, where the signal spatial extent considered for each measurement is illustrated in two dimensions by the squares. The actual volumes for the signal measurement are $7 \times 7 \times 7 \text{ mm}^3$ (**c**) and $1.2 \times 1.2 \times 0.059 \text{ mm}^3$ (**d**), and the volume for noise measurement is $1.2 \times 1.2 \times 1.2 \text{ mm}^3$ (not shown). SNR is statistically highest for both regions of signal measurement when TE = 20 ms; * $p < 0.05$.

2.3.1.2 Oxygenation-dependent studies

To confirm that the hypointense patterns are indeed of venous origin, BOLD microscopy was performed not only with an FiO_2 level of 30% but also with FiO_2 levels of 21% and 15%; corresponding systemic arterial blood oxygen saturation level (SaO_2) ranges were 90–97, 71–92, and 52–74% (95 ± 3 , 85 ± 7 and $65 \pm 8\%$), respectively, for six animals. Note that the SaO_2 calculated with human hemoglobin P_{50} was 99 ± 1 , 95 ± 3 and $85 \pm 5\%$ with FiO_2 levels of 30, 21, and 15%, respectively. Data from one oxygenation-dependent study are shown in Figure 2.2. The dark lines observed at the highest FiO_2 level (Figure 2.2a) thicken but do not lengthen as the FiO_2 levels are reduced (Figure 2.2b and c), confirming that the dark patterns in data with $\text{FiO}_2 = 30\%$ are indeed of vascular origin. Notably, some new lines appear at the reduced FiO_2 levels (arrows in Figure 2.2b and c), which are thin and appear with low contrast relative to other vascular patterns existing within comparable or shallower cortical depths. Even though it is not obvious from the 2D displays, careful evaluation of 3D data shows that these new vascular patterns appearing at reduced FiO_2 levels usually have increased contrast at deeper cortical regions, and some disappear near the cortical surface (example indicated by arrows in Figure 2.2d), indicating that blood oxygenation level decreases with cortical depth. There was no continuation of these patterns in adjacent volumes, indicating that this aspect of their appearance is not due to a partial volume effect. When $\text{FiO}_2 = 15\%$, these new vascular patterns were evident in all animals ($N = 6$, systemic $\text{SaO}_2 = 65 \pm 8\%$). When $\text{FiO}_2 = 21\%$, some of these new vascular patterns were observed in half of the animals ($N = 3$, systemic $\text{SaO}_2 = 80 \pm 8\%$), while there was no evidence in the remainder ($N = 3$, systemic $\text{SaO}_2 = 89 \pm 3\%$). Based on these characteristics, the new vascular patterns are likely of arterial origin. To minimize any potential contamination of arterial vessels, only datasets with $\text{FiO}_2 = 30\%$ were used to examine venous patterns and quantify venous density and size characteristics.

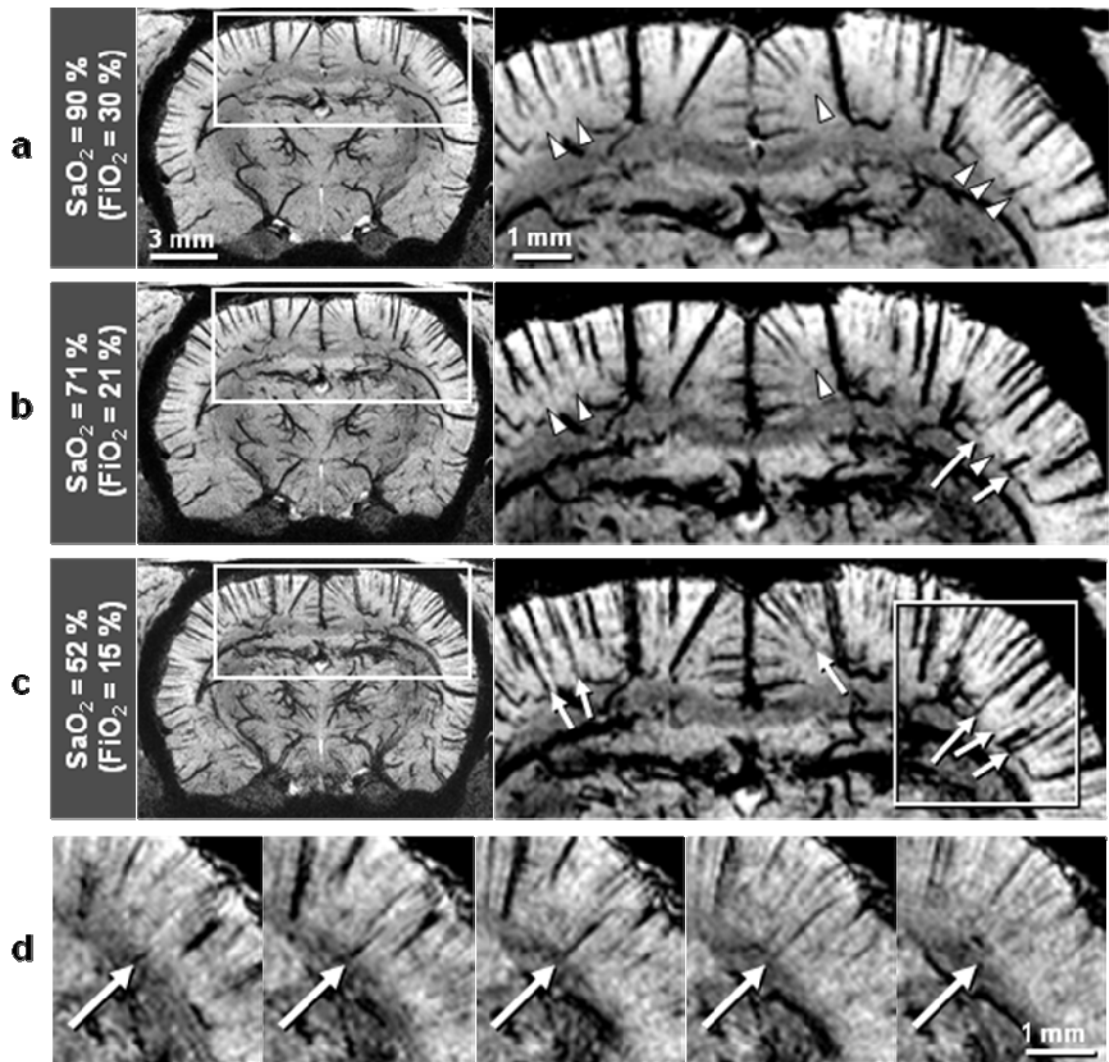


Figure 2.2 **Oxygenation-dependent 9.4-T BOLD 3D microscopy** study. Data were acquired with $TE = 20$ ms in an animal different from Figure 2.1a and b ($N = 6$ total). Displays are minimum-intensity projections of 1-mm thick coronal slabs. SaO_2 and FiO_2 in **a–c** represent values for the oxygen saturation level of systemic arterial blood and the fraction of inspired oxygen, respectively. Note that SaO_2 was calculated with the half saturation partial pressure of oxygen appropriate for rat hemoglobin. Regions within the rectangles (left) are expanded (right), with intensity and contrast levels adjusted to emphasize the SaO_2 dependence of vessels presumed to be arteries. Arterial candidates are marked when they are visible (arrows) and not yet visible (arrowheads). An arterial candidate from within the rectangular region in **c** are better visualized in expanded views of five consecutive single-pixel thick ($59\text{-}\mu\text{m}$) planes, where the long arrow indicates a vessel with increased contrast at deeper cortical regions.

2.3.1.3 Visualization of veins

Venous patterns are clearly observed when $TE = 20$ ms and $FiO_2 = 30\%$ (Figure 2.3). Key features are apparent even when venograms are displayed with only single-pixel thickness (Figure 2.3a–c). When venous vessels (veins and venules) are oriented parallel to the plane, they appear as dark lines; this is clearly seen in a coronal view where most intracortical vessels are perpendicular to the cortical surface (Figure 2.3a). When venous vessels are oriented perpendicular to the plane, they appear as dark spots, as seen in an axial view (Figure 2.3b). Pial veins at the medial surface are especially prominent in the sagittal view (Figure 2.3c). When signals were averaged across a 1-mm thick axial slab near the dorsal cortical surface, pial and intracortical veins were consistently detected (Figure 2.3f). The 59- μ m thick reconstructions also show detailed anatomical structure; gray to white matter contrast is sufficient to resolve corpus callosum and internal capsule (Figure 2.3a and b), while ventricles appear hyperintense (Figure 2.3a and c). Lateral ventricles also appear in a 59- μ m thick axial view reconstructed ~ 0.3 mm ventral to the location of Figure 2.3b (not shown).

Venous patterns become even more conspicuous in displays where minimum-intensity projection was performed over 1-mm thick slabs (Figure 2.3d and e) centered at the planes of Figure 2.3a and b. Veins are then visible not only within the cortex, but also in subcortical regions, including the thalamus and hippocampus. Intracortical venous vessels draining the deepest cortical regions generally appear to have larger diameters in these images. A few intracortical branches can be seen along some large veins (arrows in Figure 2.3d and e); this was consistently observed in all six animals.

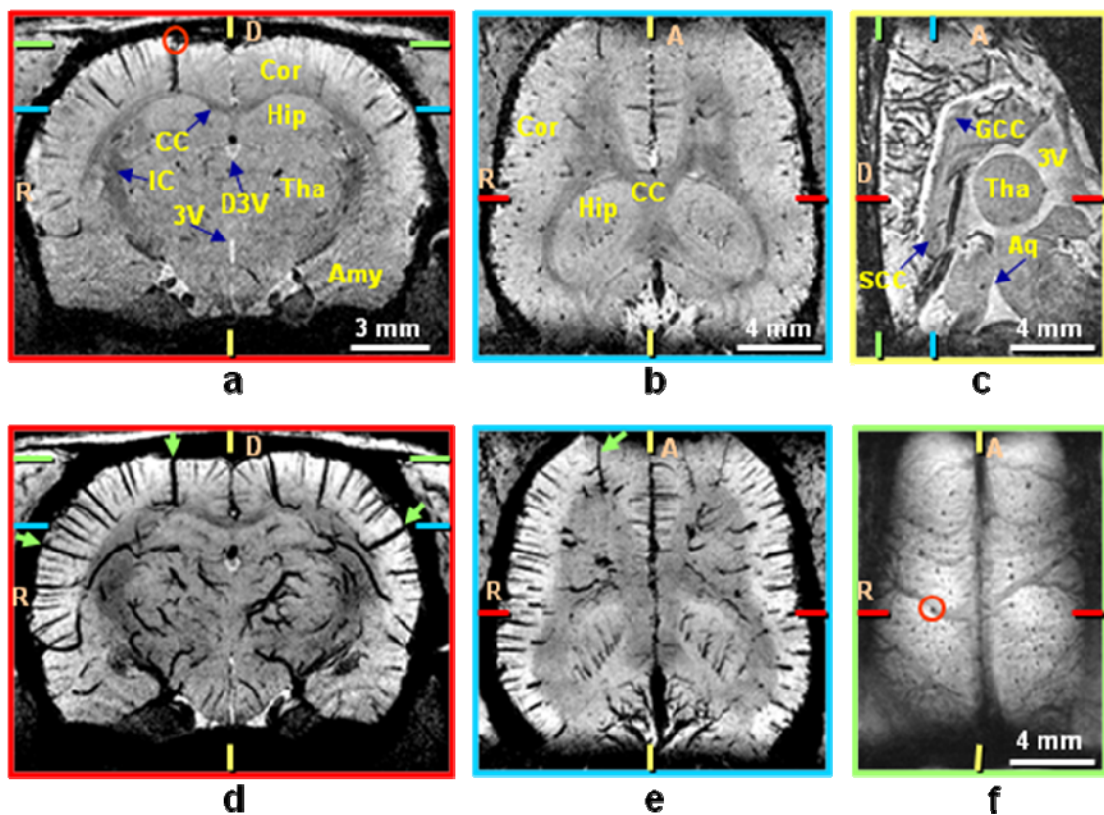


Figure 2.3 **Endogenous BOLD-contrast venograms at 9.4 T** demonstrating various 2D reconstructions from one 3D dataset. Data were acquired with TE = 20 ms and the fraction of inspired oxygen = 30% (systemic arterial oxygen saturation level = 90%) from the same animal shown in Figure 2.2. Image reconstructions from single-pixel thick (59 μ m) sections are shown along coronal (a), axial (b), and sagittal (c) directions. Minimum-intensity projections of 1-mm thick slabs are shown along coronal (d) and axial (e) directions, where projection slabs were centered at the planes of a and b, respectively. Images a and d are centered \sim 0.5 mm posterior to the reconstruction of Figure 2.2a. Green arrows in d and e indicate intracortical vessels that have visible branches. For a reconstruction from the dorsal cortical surface (f), pixels across a slab thickness of 1 mm were averaged. Colored ticks represent slice or slab centers for reconstructions with borders of the same color. The same intracortical vein (marked by small red circles) is seen in a coronal view (a) and as it drains to the cortical surface (f). A = anterior; D = dorsal; R = right; Amy = amygdala; Aq = aqueduct; CC = corpus callosum; Cor = cortex; D3V = dorsal third ventricle; GCC = genu corpus callosum; Hip = hippocampus; IC = internal capsule; SCC = splenium corpus callosum; Tha = thalamus; 3V = third ventricle.

2.3.1.4 Cortical depth-dependent venous distribution

The distribution of venous vessels as a function of cortical depth in data acquired with $TE = 20$ ms and $FiO_2 = 30\%$ is illustrated in Figure 2.4. The manually-drawn yellow curve along the middle of the cortex (Figure 2.4a) defined the location for reconstruction of a flattened plane (Figure 2.4b), where intracortical venous vessels appear as small spots due to their perpendicular orientation. Cross-sectional views at select depths within the somatosensory cortex were also reconstructed for 1.8×1.8 mm² regions (red lines and square in Figure 2.4a and b), and these are shown in Figure 2.4c–f for cortical depths of 0.1, 0.4, 1.0, and 1.6 mm, respectively. Pial veins are observed in the plane near the cortical surface (Figure 2.4c). Fewer intracortical venous vessels are visualized with increased cortical depth (Figure 2.4d–f). A histogram of the $1.8 \times 1.8 \times 0.059$ mm³ region at 0.4-mm depth (Figure 2.4g) illustrates deviation from a Gaussian fitting for pixel intensities below $\sim 85\%$ of the average tissue signal intensity; histograms of the same regions in all animals (12 hemispheres) for cortical depths of 0.4, 1.0, and 1.6 mm appear similar, with deviations occurring for pixel intensities below $84 \pm 2\%$, $86 \pm 3\%$, and $86 \pm 3\%$, respectively.

As cortical depth increases, the total density of intracortical venous vessels identified with the default criteria (intensity threshold of 85% of average tissue intensity, depth contiguity of four pixels) decreases (Figure 2.4h–j, right-most bars); differences in the total identifiable venous densities of 5.7 ± 1.0 , 3.5 ± 1.0 , and 1.5 ± 0.6 / mm² (12 hemispheres) at cortical depths of 0.4, 1.0, and 1.6 mm, respectively, were statistically significant (Wilcoxon signed rank test, $p < 0.05$). The cumulative density patterns of Figure 2.4h–j (all bars) represent distribution by venous size. Although the magnitudes are reduced, the overall pattern of the cumulative venous density plots for vessels with < 10 in-plane contiguous pixels is similar for the three cortical depths, indicating a proportionate reduction in density with cortical depth for all but the largest detectable vessels. Venous density is dependent on the choice of both intensity threshold and

depth contiguity. Criteria-based quantification was therefore evaluated for the same regions at a cortical depth of 0.4 mm – a choice based on relatively high venous density, and potential for comparison with two-photon microscopy data. When the depth contiguity criterion was fixed at 4 pixels, but the intensity threshold varied from 80% to 90% of average tissue signal intensity, the density of identifiable venous vessels of all sizes was 4.4 ± 0.6 and $8.0 \pm 1.6 / \text{mm}^2$ (12 hemispheres), respectively. When the intensity threshold was fixed at 85%, but the depth contiguity criterion varied from 3 pixels ($\sim 180 \mu\text{m}$) to 5 pixels ($\sim 300 \mu\text{m}$), the density of identifiable venous vessels of all sizes was 6.4 ± 1.3 and $5.3 \pm 0.9 / \text{mm}^2$ (12 hemispheres), respectively.

Mean FWHMin values at cortical depths of 0.4, 1.0, and 1.6 mm were 128 ± 10 , 131 ± 12 , and $141 \pm 14 \mu\text{m}$, respectively, for veins identified with the default criteria. More than 95% of identifiable venous vessels within the regions measured at each cortical depth had FWHMin values between 90 and 190 μm . Quantities representing FWHMin and the number of in-plane contiguous pixels are not inter-convertible due to inherent differences in their properties. When small vessels are not fully contained within a pixel, the resulting artificial broadening is likely to more severely affect the FWHMin value to an unknown degree.

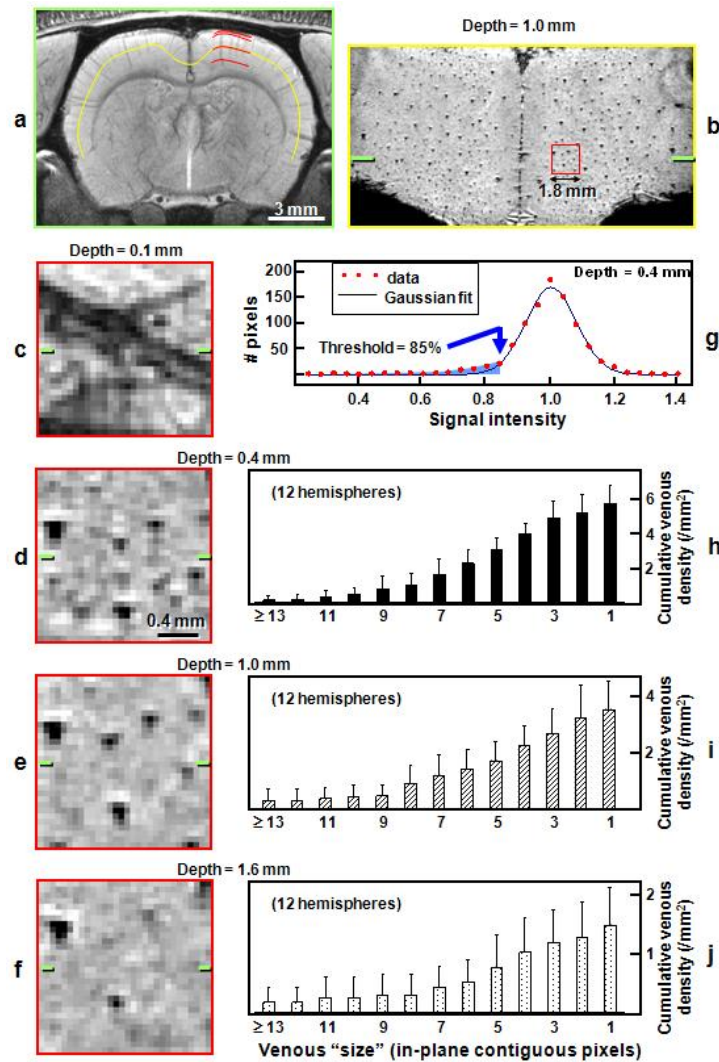


Figure 2.4 Reconstructions from a 9.4-T BOLD 3D venographic dataset and cortical depth-dependent quantification of venous distributions. Data were acquired with TE = 20 ms, and with the fraction of inspired oxygen = 30%. **a–g:** Data from one representative animal (different from Figures 2.1–2.3) (systemic arterial oxygen saturation level = 95%). **a:** Coronal view reconstructed by averaging pixels across a 1-mm thick slab. Red curves are 1.8 mm in length and indicate cortical depths of 0.1, 0.4, 1.0, and 1.6 mm, within the somatosensory cortex. **b:** A single-pixel thick (59- μ m) reconstruction at the location of the yellow curve in **a** (cortical depth of 1.0 mm). The red square in **b** represents a $1.8 \times 1.8 \text{ mm}^2$ region within the somatosensory cortex. **c–f:** Expanded views of selected $1.8 \times 1.8 \times 0.059 \text{ mm}^3$ regions at 0.1 (**c**), 0.4 (**d**), 1.0 (**e**), and 1.6 mm (**f**) from the cortical surface, as indicated by the red curves in **a**. The green ticks in **b–f** represent the slab center of **a**. **g:** Histogram of the $1.8 \times 1.8 \times 0.059 \text{ mm}^3$ region at a cortical depth of 0.4 mm (shown in **d**) and its Gaussian curve fitting. Thirty discrete intensity bins were chosen based on minimum and maximum signal intensities within the region of interest. Venous pixel candidates (blue shading) are assigned as those with the intensity threshold = 85% of average tissue signal intensity (blue arrow). **h–j:** Cumulative intracortical venous densities vs. venous “size” (expressed as minimum in-plane contiguous pixels defining each identifiable venous vessel) at cortical depths of 0.4 (**h**), 1.0 (**i**), and 1.6 mm (**j**), for all studies (12 hemispheres). The right-most bar in each plot represents total venous density, which decreases with cortical depth ($p < 0.05$). Note the independent adjustment of vertical scales for better visualization. Measurements were performed within $1.4 \times 1.4 \times 0.059 \text{ mm}^3$ regions concentric with the $1.8 \times 1.8 \times 0.059 \text{ mm}^3$ regions illustrated in **d–f**, using default criteria for venous vessel identification (intensity threshold of 85% of average tissue signal intensity and depth contiguity of 4 pixels). The measurement error in cortical depth due to spatial variation of the cortical surface is $\sim 0.1 \text{ mm}$ ($N = 6$).

2.3.2 Two-photon Microscopy Studies

The SaO₂ ranges for five animals used for two-photon microscopy studies were 90–97% (92 ± 4%). Detailed intracortical vasculatures including capillaries are visualized in the two-photon microscopy data (see Figure 2.5a). Images obtained at cortical depths of 0.1 and 0.4 mm (Figure 2.5b and c) represent details not detectable in the MRI data. Cross sections of intracortical venous vessels that are perpendicular to the cortical surface have round profiles (e.g., Figure 2.5b and c, arrows), where diameters were measured. The slopes in the cumulative venous density plots for cortical depths of 0.1 and 0.4 mm (Figure 2.5d-e) indicate a large population of relatively small venules (~10–30 μm diameter) compared to larger venous vessels in intracortical vasculature. At cortical depths of 0.1 mm and 0.4 mm, mean diameters of 23 ± 12 μm (96 venous vessels from 5 animals) and 17 ± 10 μm (59 venous vessels from 5 animals), respectively were statistically different ($p < 0.05$). Note that only vessels traceable to the cortical surface for venous/arterial assignment were measured and therefore the smallest vessels are greatly underrepresented. The total venous densities at cortical depths of 0.1 and 0.4 mm were 23.2 ± 2.9 / mm² and 14.2 ± 4.0 / mm² (Figure 2.5d-e, right-most bars), respectively, which were also statistically significant (Wilcoxon signed rank test, $p < 0.05$). Mean venous densities for vessels with diameter > 10, 15, 20, 25, and 30 μm were 11.1 ± 3.9, 5.3 ± 1.8, 3.4 ± 1.6, 2.7 ± 1.6, and 1.5 ± 1.6 / mm² at a cortical depth of 0.4 mm (Figure 2.5e), respectively.

\

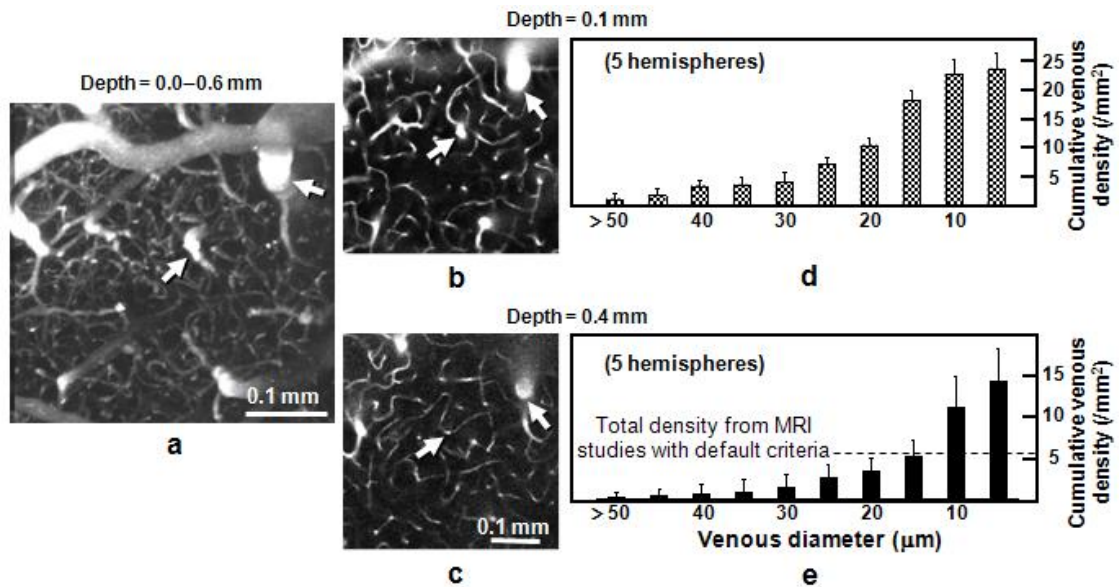


Figure 2.5 Images from a 3D *in vivo* two-photon angiographic dataset and cortical depth-dependent quantification of venous distributions. a–c: Data from one animal. The ability of this *in vivo* technique to resolve intracortical arteries and veins with much finer detail than by BOLD venography is illustrated in the maximum-intensity projected reconstruction ($0.456 \times 0.456 \times 0.6 \text{ mm}^3$) along the axial direction (a), where complete vascular networks including capillaries with $\sim 5\text{-}\mu\text{m}$ diameter are observed. Two-dimensional single plane images ($0.456 \times 0.456 \text{ mm}^2$) parallel to the surface at cortical depths of 0.1 mm (b) and 0.4 mm (c) show that relatively large sized vessels perpendicular to the cortical surface appeared as round shapes. Intracortical veins (and also arteries) can be traced between the surface and deep cortical regions, as seen in examples indicated by arrows. Note that these two-photon microscopy images (b and c) represent only $\sim 1/16$ the area as compared to the MRI venograms of Figure 2.4c–f. Cumulative intracortical venous densities (expressed as minimum venous diameter) are plotted as a function of diameter at cortical depths of 0.1 (d) and 0.4 mm (e) for all studies ($N=5$). The right-most bar in each plot represents total venous density, which decreases with cortical depth ($p < 0.05$). Vertical scales were independently adjusted for better visualization. The density of smaller-diameter venous vessels (10–30 μm) is higher than that of larger-diameter vessels at both cortical depths. Density at 0.4-mm depth for intracortical venous vessels with diameter $\geq 15 \mu\text{m}$ is $5.3 \pm 1.8 / \text{mm}^2$, which roughly corresponds to the venous density measurement of $5.7 \pm 1.0 / \text{mm}^2$ from our MRI data at the same depth using the default criteria (broken line). Note that due to a small field of view of two-photon microscopy, the two-photon densities were quantified for regions covering roughly half the area as compared to MRI data.

2.4 DISCUSSION

2.4.1 Contrast in BOLD venograms

A longer echo time improved contrast in 9.4-T BOLD venograms, by limiting noise due to the correspondingly narrower acquisition bandwidth (i.e. enhancing SNR of tissue and thus CNR between tissue and blood) and by extending the susceptibility effect of dHb further into the surrounding tissue (Figure 2.1). Empirical results of the TE-dependent studies also match theoretical expectations. Tissue signal intensity depends on $\exp(-TE/T_{2,t}^*)$, where $T_{2,t}^*$ is the T_2^* value from tissue, while the noise level depends on $(T_{\text{read}})^{-1/2}$. Therefore tissue SNR is dependent on $\exp(-TE/T_{2,t}^*) \cdot T_{\text{read}}^{1/2}$, where TE in our studies is $(T_{\text{delay}} + T_{\text{read}})/2$. Tissue SNR is highest when T_{delay} is minimized (5 ms) and $T_{\text{read}} = T_{2,t}^*$ (as seen by differentiation with respect to T_{read}). In our experiments, $T_{2,t}^*$ values were found to be 31.4 ± 1.5 ms (large brain region in Figure 2.1c) and 35.0 ± 0.6 ms (small cortical region in Figure 2.1d) ($N = 6$). Thus, optimal SNR will be achieved when T_{read} is 31.4–35.0 ms and the corresponding TE is 20.7–22.5 ms, which agrees with our experimental findings (Figure 2.1c and d). Because the optimal TE value for 9.4-T BOLD microscopy is relatively long, the minimum-phase Shinnar-Le Roux RF pulse used here to test TE-dependence could be replaced with any RF pulse.

The effect of phase-contrast filtering (6,7,18,20) to enhance susceptibility weighting for 9.4-T BOLD microscopy was examined with our rat brain data obtained for all five TE values at $\text{FiO}_2 = 30\%$ after removing variations in the phase datasets due to static field inhomogeneity with a high-pass filtering algorithm (19). Contrast was enhanced for some venous patterns, but there was little improvement in their overall detectability with phase-contrast filtering, unlike the improvements seen at low fields (6,7,18). Phase-contrast filtering at 9.4 T also introduced

significant susceptibility artifacts at regions near air/tissue/bone interfaces, which were more severe at longer TE values. These observations were consistent in all six animals. Although the effect of phase-contrast filtering at 9.4 T may be debatable, the lack of distortion in images without phase-contrast filtering appears to make them preferable. Further optimization and systematic analyses are required to determine the utility of high-field phase-contrast filtering.

2.4.2 Threshold level for venous identification

Our choice of 85% of the average tissue signal intensity as the threshold level for positive assignment of venous vessels was based on the following reasons. According to literature (40), a CNR value of ~ 5 is required for reasonable discrimination. CNR between tissue and venous blood can be expressed as $\Delta S/\sigma = (\Delta S/S_t) \cdot (S_t/\sigma) = (\Delta S/S_t) \cdot \text{SNR}$, where ΔS represents the signal difference between venous blood and tissue, S_t is the average tissue signal intensity, and σ is noise, i.e. the standard deviation of signal. Since $\Delta S/S_t$ at an 85% threshold level is 0.15, and SNR of tissue in a region without prominent vessels at TE = 20 ms is 35.8 ± 5.4 (Figure 2.1d), the resultant CNR is 5.37 ($= 0.15 \times 35.8$), meaning our intensity threshold criterion is reasonable. Our choice of threshold level is also supported by the observation that histograms of the cortical depth-dependent $1.8 \times 1.8 \times 0.059 \text{ mm}^3$ regions have a non-Gaussian distribution for signal intensities below $\sim 85\%$ of the average tissue intensity (example in Figure 2.4g), which seems to indicate contributions from the hypointense pixels containing venous vessels.

2.4.3 Minimum-detectable Vessel Size in BOLD Microscopy

Detectability of venous and arterial vasculature can be roughly estimated by comparing BOLD microscopy patterns to two-photon microscopy diameter measurements. Intracortical *venous* diameters measured by our two-photon microscopy studies were $< 80 \mu\text{m}$ (data not shown).

According to *in vivo* measurements of pial venous diameters, with every increase in venous branching order in the cortex, venous diameter decreases by a factor of ~ 2 (41). The analogous relationship indicates the first branches off from the largest intracortical veins (one increase in branching order) may have diameters of $< 40 \mu\text{m}$ (i.e., half of $< 80 \mu\text{m}$). In our BOLD microscopy data, when systemic SaO_2 values are 90–97%, these branches were indeed detected (see Figure 2.3d and e). Systemic venous oxygen saturation levels measured in separate animals under the same conditions were $50 \pm 3\%$ ($N = 2$) (equivalent to 71% with the human hemoglobin P_{50} value for calculation). It is therefore reasonable to assume that venous vessels with diameter $< 40 \mu\text{m}$ are detectable under our experimental conditions, when systemic venous and arterial oxygenation levels are ≤ 50 and 90%, respectively. Intracortical *arterial* diameters measured in our two-photon microscopy studies were $< 40 \mu\text{m}$ (data not shown). In our BOLD venograms, new vascular patterns that were likely of arterial origin (arrows in Figure 2.2c and d) appeared when systemic SaO_2 values were less than 80%, indicating that intracortical vessels with diameters $< 40 \mu\text{m}$ may be detectable under these conditions.

To better assess detectability of venous vasculature, BOLD microscopy densities were compared with actual diameter-dependent densities measured by two-photon microscopy. Density for all venous vessels detected by BOLD microscopy for our conditions at 0.4-mm depth in the somatosensory cortex was $5.7 / \text{mm}^2$ for default criteria for intensity threshold and depth contiguity and $8.0\text{--}4.4 / \text{mm}^2$ over the range of criteria tested; comparison with two photon data at the same depths shows a venous detectability of $\sim 15\text{--}10 \mu\text{m}$ and $10\text{--}20 \mu\text{m}$, respectively. This correspondence implies that our BOLD microscopy may detect venous vessels at least as small as $20\text{--}10 \mu\text{m}$ diameter. But, since different animal groups were used for MRI and two-photon studies, there may be some errors in matching cortical depths between the two modalities. Inspection of two-photon microscopy data in Figure 2.5d and e shows that cumulative density decreases for vessels of all sizes as cortical depth increases. Thus, a more conservative estimate of MR vessel

detectability can be obtained by comparing venous density from MRI studies measured at 0.4-mm depth with the cumulative densities from two-photon studies measured at 0.1-mm depth (Figure 2.5d); BOLD microscopy venous densities of 5.7 /mm² for default criteria and 8.0–4.4 /mm² for the range of criteria tested then correspond to conservative detectability estimates of 25–30 μm and 20–30 μm, respectively.

FWHMin values of intracortical veins identifiable in our MRI studies were mostly 90–190 μm, indicating that the extended susceptibility effect of dHb into surrounding tissue makes veins appear to be more than triple their actual size under our experimental conditions. This exaggerated size compares favorably with previous blood-filled vascular phantom studies at 7 and 8.4 T by Ogawa et al. (4,5). It should be noted that the spatial extent of signal dephasing induced by the susceptibility effect of dHb is dependent on many parameters determined by experimental conditions (TE, magnetic field strength, and voxel resolution) and physiology (blood oxygenation level, hematocrit level, and vessel size and orientation).

To obtain further insight into vessel detectability at 9.4 T as a function of local oxygen saturation level and signal intensity threshold, computer simulations were performed based on a cylinder model of a single blood vessel perpendicular to both the main magnetic field and imaging plane (18,20,21,42). The area defined by in-plane resolution in these 2D simulations is denoted here as a “pixel”. Signal intensity of a pixel containing varying portions of a single vein (relative to pixel intensity without any venous contribution) was calculated for our experimental conditions as a function of vessel diameter, by considering magnitude and phase of both intra- and extra-vascular spins within the pixel. Signal intensity is dependent on the partial volume fraction of venous blood (which is related to the position of the vein within the pixel), and thus the condition with the lowest partial blood volume fraction (i.e., when the center of the venous vessel is located at a corner of the pixel) was chosen for our simulation of minimum detectability. Parameters for the simulation were T_1 of tissue and venous blood = 1.9 and 2.2 s,

respectively (43); tissue $T_2^* = 35$ ms; venous $T_2^* = 4.0, 4.9, 6.4, 9.0,$ and 15.2 ms for oxygen saturation levels of 50, 60, 70, 80, and 90%, respectively (22) (based on venous T_2 values measured in rat brain with different oxygen saturation levels calculated by human blood gas analyzer); relative spin density of tissue and venous blood = 0.89 and 0.86 (44); hematocrit level = 0.4; and susceptibility difference between fully oxygenated and deoxygenated blood = 0.2×10^{-6} in cgs units (21,45). For local oxygen saturation levels of 50, 60, 70, 80, and 90%, minimum-detectable vessel diameters for our conditions (e.g. TE = 20 ms, in-plane resolution = $78 \times 78 \mu\text{m}^2$, etc.) are 20, 22, 25, 30, and 48 μm when the intensity threshold is 85% of tissue signal intensity, respectively; the diameters are 23, 26, 30, 36, and 56 μm at the intensity threshold of 80%, respectively, and 16, 18, 20, 25, and 39 μm at the intensity threshold of 90%, respectively. Only systemic oxygen saturation levels were measured, but if it is assumed that local and systemic venous oxygen saturation levels are similar, then local venous oxygen saturation levels are $50 \pm 3\%$ (when measured systemic SaO_2 values were 90–97%). Our simulations therefore indicate that vessels with diameters as small as 16–23 μm can be detected in our venograms when the local oxygen saturation level is $\leq 50\%$.

In summary, both simulation results and density measurement comparisons between the two different imaging modalities (BOLD-based and two-photon microscopy) make it reasonable to conclude that venous vessels with diameters as small as $\sim 16\text{--}30 \mu\text{m}$ are detectable by 9.4-T BOLD microscopy under our experimental conditions.

3.0 COMPATIBLE DUAL-ECHO ARTERIOVENOGRAPHY (CODEA) USING AN ECHO-SPECIFIC K-SPACE REORDERING SCHEME BASED ON TIME-OF-FLIGHT (TOF) AND BLOOD OXYGENATION LEVEL-DEPENDENT (BOLD) EFFECTS

3.1 INTRODUCTION

MR angiography that is based on the time-of-flight (TOF) contrast (8) provides detailed anatomy of arterial vasculature and is routinely used in clinical brain imaging. As a complementary vascular imaging modality, MR venography that is based on blood oxygenation level-dependent (BOLD) contrast (4,5) has been performed and used clinically to delineate venous anatomy in the brain (7,46-48). Because TOF MR angiogram (MRA) and BOLD MR venogram (MRV) depict different neuronal and vascular abnormalities in brain diseases, it is desirable to acquire both of them in clinical brain imaging studies. Nevertheless, both MRA and MRV require relatively long scan durations, typically 5–15 minutes for each method. Accordingly, acquisition of both MRA and MRV in routine clinical brain imaging studies would increase the total imaging time, reduce the examination throughput, and possibly limit patient's compliance. As a result, MRV is not routinely obtained in clinical brain imaging examinations.

Recent studies have reported new technical developments relating to the simultaneous acquisition of both TOF MRA and BOLD MRV using the scan time required for only one, MRA or MRV (24,49). Despite this considerable advance, technical challenges remain in the simultaneous acquisition of MRA and MRV due to conflicting scan conditions required for the

optimization of MRA and MRV. On one hand, the MR angiography necessitates the application of a ramped excitation pulse with higher flip angle (24,49), magnetization transfer contrast (MTC) pulse (14,15), spatial presaturation pulse, and shorter echo time (TE) for better inflow enhancement. On the other hand, the MR venography requires a flat excitation pulse with lower flip angle, no preparation pulse, a longer TE, and a low acquisition bandwidth for better T_2^* contrast. These conflicting scan parameter requirements for the optimization of MRA and MRV are not readily counter-balanced or reconciled in the previously-reported methods for simultaneous acquisition of MRA and MRV. For example, in the dual-echo method proposed by Du and Jin (24), the RF pulse conditions (i.e., excitation RF profile, flip angle, spatial presaturation pulse, MTC pulse) were not adjustable between the acquisitions of MRA and MRV. Consequently, the vascular contrast of the MRA and MRV could not be optimized. In the MRA, the arteries are depicted by virtue of their hyperintense signal, and the background tissue signal should be suppressed. The opposite is true in the MRV. To accommodate these conflicting requirements, the dual-echo scan parameters for the MRA and MRV should be individually adjustable.

Dual-echo scan parameters compatible for both the MRA and MRV vascular contrast can be achieved by exploring K-space characteristics and employing an echo-specific K-space reordering scheme. In particular, because the tissue contrast is determined predominantly by the K-space center characteristics, the vascular contrast for the MRA and MRV can be enhanced by maximally separating the K-space center region acquired for the MRA from that for the MRV. Pursuant to the echo-specific K-space reordering scheme, the scan parameter requirements for the MRA and MRV can be uncoupled and adjusted independently. The purpose of our study was to develop and implement compatible dual-echo arteriovenography (CODEA) for simultaneous acquisition of TOF MRA and BOLD MRV in a single MR acquisition.

3.2 THEORY

3.2.1 Excitation RF pulses

As the spins of the flowing blood penetrate more distally downstream in an imaging slab, they repeatedly experience more RF excitations, and gradually saturate. The blood signal in 3D TOF MRA thus saturates and decreases proportional to its spatial location, from the upstream to the downstream, within an imaging slab. This RF spatial saturation can be compensated and reversed by the application of an excitation RF pulse with a spatially-varying ramp profile (TONE: tilted optimized nonsaturating excitation (9,10)). In our study, a minimum-phase RF pulse (to minimize TE for MRA) with a spatially-varying ramp profile was designed following the Shinnar Le-Roux algorithm (11) (Figure 3.1a). The excitation profile was simulated and tested by a Runge-Kutta embedded numerical solution of the Bloch equations (50) (Figure 3.1b).

Compared to the arterial blood, the BOLD-based MRV vascular contrast is less likely to depend on blood movement. Furthermore, the ramped RF pulse may cause spatially-varying uneven background tissue signal intensity in the MRV. For these reasons, an excitation RF pulse with a flat profile is preferred in the MRV. The aforementioned ramped RF pulse consists of the real and imaginary parts (darker and lighter gray lines, respectively, in Figure 3.1a), and the real part corresponds to the conventional minimum-phase Shinnar Le-Roux pulse, which generates a flat excitation profile (darker gray line in Figure 3.1b). In our dual-echo sequence implementation, therefore two different RF pulses were used for each of the MRA and MRV: one RF pulse with a ramped profile containing both the real and imaginary parts for the first echo (MRA), and the other RF pulse with a flat profile containing only the real part for the second echo (MRV). These

two RF pulses were applied at two separate K-space regions in a 3D dataset, while the slab-select and refocusing gradients remained the same.

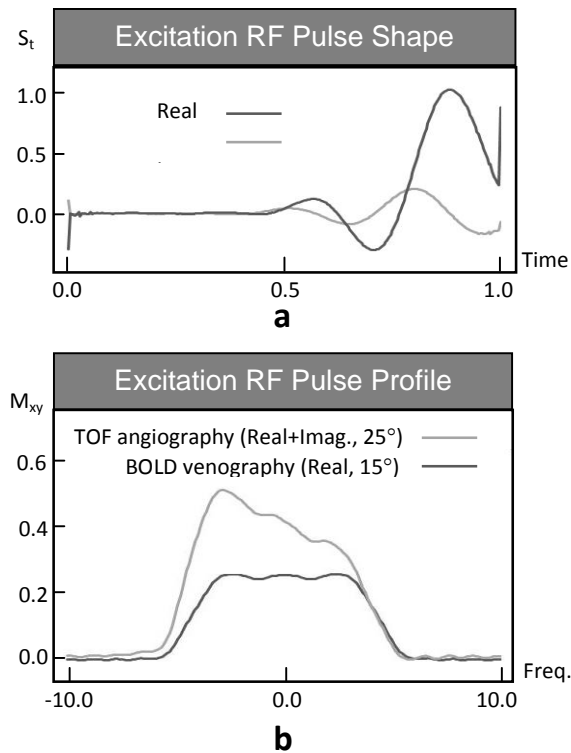


Figure 3.1 **Excitation RF pulse shape and profile used in TOF MRA and BOLD MRV.** **a:** Shapes of real and imaginary parts of the minimum phase RF pulse with ramped excitation profile. **b:** Two different excitation RF pulse profiles. One RF pulse, consisting of both the real and imaginary parts of the RF pulse with the flip angle of 25° , was used for TOF MRA (both single- and dual-echo acquisitions). The other RF pulse, consisting of only the real part of the RF pulse with the flip angle of 15° , was used for BOLD MRV (again both single- and dual-echo acquisitions).

3.2.2 CODEA with echo-specific K-space reordering scheme

The pulse sequence diagram for CODEA is shown in Figure 3.2. First-order flow compensation was applied to both the slab-select and readout gradients (15,16,24). According to our echo-specific K-space reordering scheme, the 1st and 2nd phase-encoding (PE) gradients in the second echo were designed and applied independently from those in the first echo (i.e., rewound and applied again in the middle). To enhance vascular-specific tissue contrast, the MRA and MRV were subjected to two different RF pulse-related settings (excitation pulse profile, flip angle, spatial presaturation pulse, and MTC pulse). This application of the echo-specific RF pulse-related parameters is not feasible in a dual-echo setting when the first echoes for MRA and the second echoes for MRV are acquired at the same K-space lines. The K-space acquisition ordering was altered, therefore, from the conventional (sequentially-ascending) K-space ordering. The initial $\frac{1}{4}$ of the K-space lines for the first echo were acquired at the end, while the final $\frac{1}{4}$ of the K-space lines for the second echo were acquired at the beginning along the 1st PE axis, as shown in Figure 3.3a and b (unless specified otherwise). This reordered K-space acquisition scheme allowed the K-space center regions for the two echoes to be maximally separated in this direction (*in vivo* data in Figure 3.3a and b). Consequently, the RF pulse-related parameters for the MRA could be applied during the acquisition of the center half of the first-echo K-space (TOF-weighted region); those for the MRV, during the acquisition of the center half of the second-echo K-space (BOLD-weighted region) (Figure 3.3). Hence, the peripheral half of K-space (i.e., $\frac{1}{4}$ on each side) of one echo was weighted by the RF pulse parameters designated for the other echo. Because the 1st PE direction typically had a higher spatial resolution (K-space lines with higher frequencies) than the 2nd PE direction, the K-space acquisition was reordered along the 1st PE direction to increase the K-space separation between the two echoes (Figure 3.3). Note that the 1st PE loop was located outside the 2nd PE loop in order to minimize any potential perturbations in

the steady-state condition (Figure 3.2). In this way, the RF pulse parameters were switched only once midway through the scan without a transitional period of dummy RF pulses during the acquisition of an entire 3D dataset.

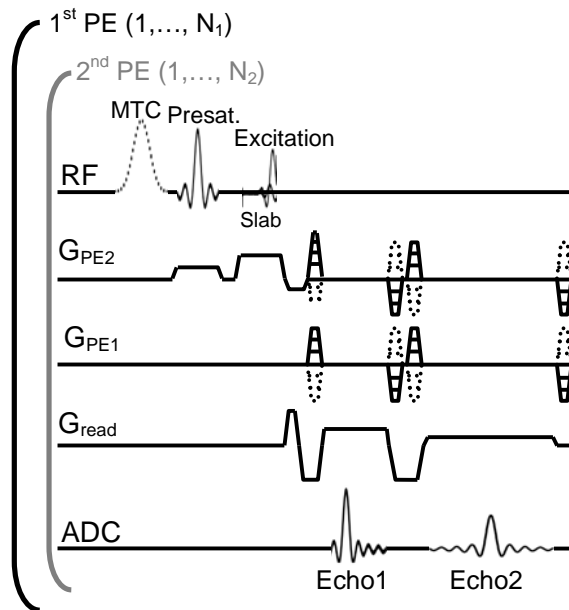


Figure 3.2 **Pulse sequence diagram for CODEA.** The diagram is for the acquisition of K-space center regions of the first echo, without including spoiler gradients for simplicity. A minimum phase RF pulse was used to keep the TE of the first echo as short as possible. According to our echo-specific K-space reordering scheme, the 1st and 2nd phase-encoding gradients in the second echo were designed and applied independently from those in the first echo, i.e., rewind and applied again in the middle. Partial and full echoes were acquired for the first and second echoes, respectively. The magnetization transfer contrast (MTC) pulse was applied instead of the presaturation pulse only in one of the 3D datasets per subject. In the K-space center region in the second echo, only the real part of the excitation pulse was applied with no spatial presaturation pulse and no MTC pulse. The 1st phase-encoding loop was located outside the 2nd phase-encoding loop to minimize perturbations in the steady state condition, where N_1 and N_2 represent the total number of 1st and 2nd phase-encoding lines, respectively.

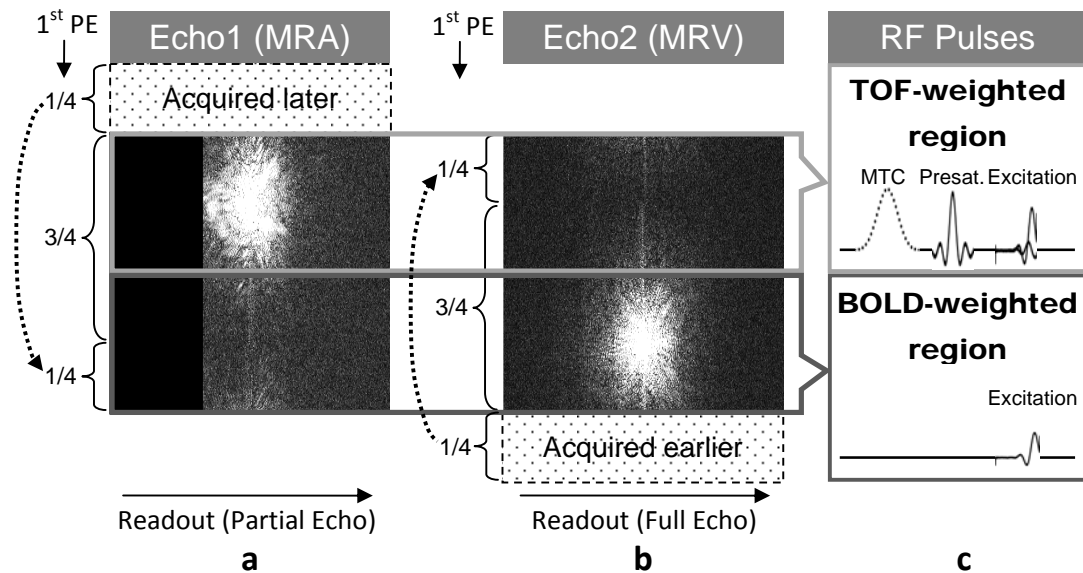


Figure 3.3 **K-space distribution of CODEA.** **a** and **b**: Cross sections of K-spaces at the center along the 2nd phase-encoding direction for the first (**a**) and the second (**b**) echoes. The K-space acquisition order was modified from the conventional, linearly-increasing order along the 1st phase-encoding direction. The initial $\frac{1}{4}$ of the total phase-encoding lines for the first echo were acquired at the end and the last $\frac{1}{4}$ of the total phase-encoding lines for the second echo were acquired at the beginning, as shown in **a** and **b**. **c**: RF pulses used for acquisition of each K-space region. When the K-space center region in the first echo was acquired (TOF-weighted MRA region), the excitation pulse with a spatially-varying ramp profile and a higher flip angle (20° – 30°) and the spatial presaturation pulse (or the MTC pulse if specified) were applied to enhance the arterial contrast in the first echo. When the K-space center region in the second echo was acquired (BOLD-weighted MRV region), the excitation pulse with a flat profile and flip angle of 15° was applied with no preparation pulse to improve the venous contrast in the second echo. Partial-echo and full-echo acquisitions were applied for the first and second echoes, respectively, as shown in **a** and **b**.

3.3 METHODS

All experiments were performed on a 3T whole-body scanner (Siemens Medical Solutions, Erlangen, Germany). Three normal male volunteers who provided informed consent were scanned in this study approved by the Institutional Review Board. Voxel-localized shimming was performed with a vendor-supplied shim module based on a 3D phase map. A total of six 3D datasets were acquired with imaging times of approximately 1 hour in each subject: four dual-echo MRA and MRV and two single-echo MRA and MRV, with varying numbers of acquisition slabs, K-space reordering schemes, and with and without an MTC pulse.

3.3.1 Single-slab, dual-echo arteriovenography (CODEA)

A single-slab, dual-echo arteriovenogram was acquired using the K-space reordering scheme (Figure 3.3). Imaging parameters were: repetition time (TR) = 50 ms, matrix size = $512 \times 208 \times 64$, corresponding field of view = $220 \times 179 \times 88 \text{ mm}^3$, and number of averages = 1. Partial Fourier sampling (75%) was employed to reduce the scan time and slice oversampling (18%) to avoid a wrap-around artifact, both of them along the 2nd PE direction. The scan time for a 3D dataset was 9.8 min. The TE and acquisition bandwidth were 3.2 ms and 150 Hz/pixel, respectively, in the first echo, and 24 ms and 34 Hz/pixel, respectively, in the second echo. Partial echo sampling (67%) was used in the first echo to reduce TE, while full echo sampling in the second echo to improve SNR. The K-space center region in the first echo (TOF-weighted region in Figure 3.3) was acquired with a ramped-profile excitation RF pulse with flip angle of 25° (20° – 30° , unless specified otherwise) (lighter gray line in Figure 3.1b) and with a spatial presaturation pulse. Both the real and imaginary parts of the RF pulse (darker and lighter gray lines in Figure 3.1a) were

used in this acquisition. On the other hand, the K-space center region in the second echo (BOLD-weighted region in Figure 3.3) was acquired with a flat-profile excitation RF pulse with flip angle of 15° (darker gray line in Figure 3.1b). Only the real part of the RF pulse (darker gray line in Figure 3.1a) was used in the second-echo K-space acquisition. The MTC pulse was not used so as to keep the specific absorption rate (SAR) low, unless specified otherwise. The utility and effect of an MTC pulse was tested separately in a later dual-echo sequence.

3.3.2 Conventional single-slab, single-echo MR angiography and MR venography

As the comparison reference to CODEA MRA/MRV, the conventional single-echo TOF MRA and single-echo BOLD MRV were acquired in two separate imaging sessions. The scan parameters of the single-echo MRA were identical to those for the first echo (TOF-weighted regions) of the CODEA and applied to the entire single-echo K-space. Likewise, the scan parameters of the single-echo MRV were the same as those for the second echo (BOLD-weighted regions) of the CODEA, and again applied to the entire single-echo K-space.

3.3.3 Multi-slab CODEA

One of the advantages of the CODEA technique is to provide multi-slab, dual-echo MRA and MRV with seamless vascular continuity over a large coverage of the brain anatomy. To demonstrate this capability, CODEA MRA/MRV was acquired in two overlapping slabs according to the multiple overlapping thin-slab acquisition (MOTSA) mode, which is commonly used in 3D TOF MRA (13). The scan parameters were similar to those for the single-slab CODEA except for the matrix size = $512 \times 208 \times 32$, corresponding field of view =

220×179×44 mm³, and acquisition of two overlapping slabs with gap between the two slabs of –5 mm. In the multi-slab CODEA, the imaginary part of the ramped excitation RF pulse (for the TOF-weighted regions) was reduced by half, thus decreasing the first-echo flip angle range from 20°–30° to 22.5°–27.5°. This reduction would improve the vascular intensity continuity between the slabs.

3.3.4 Multi-slab, dual-echo arteriovenography without K-space reordering

The aforementioned double-slab, dual-echo MOTSA *with* the echo-specific K-space reordering (CODEA) was compared to the double-slab, dual-echo MOTSA *without* the K-space reordering. In the absence of the K-space reordering, the K-spaces of both echoes were acquired according to the conventional, sequentially-increasing PE mode. The excitation RF profile was flat with the flip angle of 20° which was an intermediate value between those for the first (25°) and second (15°) echoes. No spatial presaturation pulse was applied to either echo. The remaining scan parameters were identical to the double-slab, dual-echo MOTSA with the echo-specific K-space reordering. The final scan setting was similar to that reported by Du and Jin (24), except for two different acquisition bandwidths in the two echoes and for the acquisition of a full echo for the second echo.

3.3.5 Single-slab CODEA with MTC pulse

A single-slab CODEA MRA/MRV was additionally acquired with an MTC pulse and TR of 58 ms. The other scan parameters were the same as those for the aforementioned single-slab CODEA without an MTC pulse. No spatial presaturation pulse was applied for this acquisition.

3.3.6 Reconstruction and data analysis

Each 3D raw dataset was Fourier-transformed to generate isotropic 3D images with the matrix size of $512 \times 416 \times 204$ for the single-slab acquisition and $512 \times 416 \times 102$ for the multi-slab (double-slab) acquisition, using the zero filling procedure. Venous contrast in the single- and dual-echo MRVs was enhanced using phase-mask filtering (6). To examine the effects of the MTC pulse on the CODEA MRA/MRV, the signal to noise ratio (SNR) of tissue in the single-slab datasets without and with the MTC pulse was computed by measuring the signal intensities over a tissue region devoid of detectable blood vessels and the background region outside the brain. MRA images were displayed in maximum-intensity projections, whereas MRV images in minimum-intensity projections.

3.4 RESULTS

3.4.1 Single-slab CODEA MRA/MRV vs Conventional single-slab, single-echo MRA/MRV

The MR angiograms acquired using the CODEA technique were qualitatively comparable to those using the single-echo technique for all subjects (Figure 3.4). A slight reduction in the vascular contrast was observed in some small downstream arteries (arrows in Figure 3.4e). The vascular signal intensity shown in the sagittal and coronal projection images (Figure 3.4e and f) was relatively uniform throughout the direction of blood movement, indicating that the expected signal degradation due to blood saturation was well compensated by the application of the ramped excitation pulse only to the K-space center region. In either CODEA or single-echo MRA, the spatial presaturation pulse was effective in suppressing venous signals (Figure 3.4), accentuating the hyperintense arterial signal.

MRV images acquired with the single echo and CODEA at three different positions are shown in Figure 3.5. The CODEA and single-echo MRVs were also qualitatively equivalent for all study subjects, even in the locations closer to the slab edge (Figure 3.5f) where the flip angle difference between the K-space center and edge regions was the highest (Figure 3.1b). The results suggest that the characteristics of the second echo in the CODEA MRV were predominantly determined by the flat excitation pulse applied only to the central K-space region.

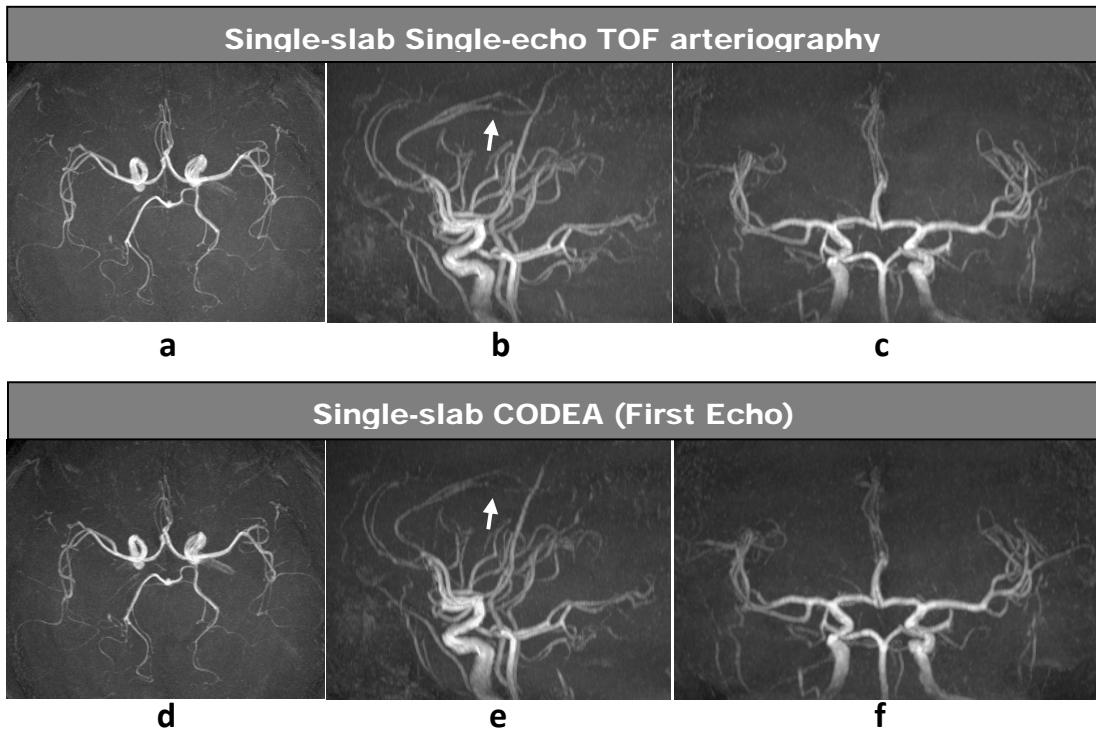


Figure 3.4 **Comparison of TOF angiograms acquired using the conventional single-echo and the CODEA methods.** **a–c:** The conventional single-echo TOF angiograms at MIP along axial (**a**), sagittal (**b**), and coronal (**c**) directions over the entire 3D volume. **d–f:** The (first-echo) CODEA TOF angiograms at MIP along axial (**d**), sagittal (**e**), and coronal (**f**) directions again over the entire 3D volume. Scan resolution for all the angiograms is $0.43 \times 0.86 \times 1.4$ (mm³). Overall, the conventional single-echo and CODEA MRAs were comparable in image quality. The arrows in **b** and **e** identify a small downstream artery with a reduced vascular contrast in the CODEA MRA.

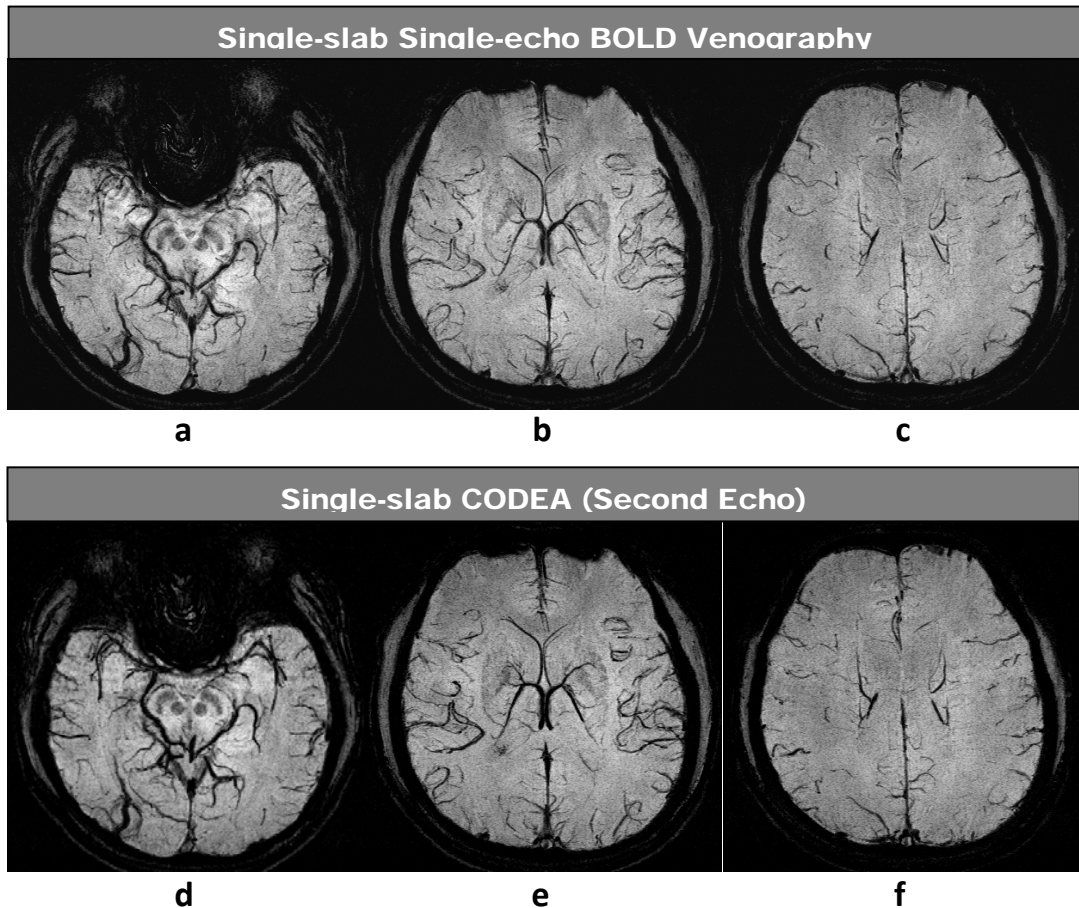


Figure 3.5 Comparison of BOLD venograms acquired using the conventional single-echo and the CODEA methods for the same subject as Figure 3.4. **a–c**: The conventional single-echo BOLD venogram at three different locations. **d–f**: The (second-echo) CODEA BOLD venogram at the same locations as **a–c**. The scan resolution for all the angiograms is $0.43 \times 0.86 \times 1.4$ (mm³). All images are minimum-intensity projections over a slab with 10-mm thickness. The conventional single-echo and CODEA MRVs were equivalent in image quality.

3.4.2 Multi-slab CODEA MRA/MRV vs Multi-slab dual-echo MRA/MRV without K-space reordering

Multi-slab (double-slab) CODEA MRA demonstrated uniform signal intensity and seamless vascular continuity in the overlapping and adjacent slices in the slabs (arrows in Figure 3.6a), while the MRA acquired without K-space reordering showed spatially-varying signal intensities in the same area (arrows in Figure 3.6c). This signal intensity variation was likely due to the downstream spin saturation effect that could not be compensated with the flat excitation pulse. Two additional drawbacks of the MRA without the K-space reordering observed in all our tested subjects were a reduced vascular contrast (because of decreased inflow enhancement with the intermediate flip angle) and signals from large veins (which could not be eliminated without an appropriate spatial presaturation pulse) (arrowhead in Figure 3.6c).

Unlike the MRA, no considerable differences in MRV image quality were observed between the double-slab CODEA (Figure 3.6b) and double-slab dual-echo arteriovenography without K-space reordering schemes (Figure 3.6d). The two techniques demonstrated equally uniform and continuous MRV signal intensity in the overlapping and adjacent vessels (arrows in Figure 3.6b and d).

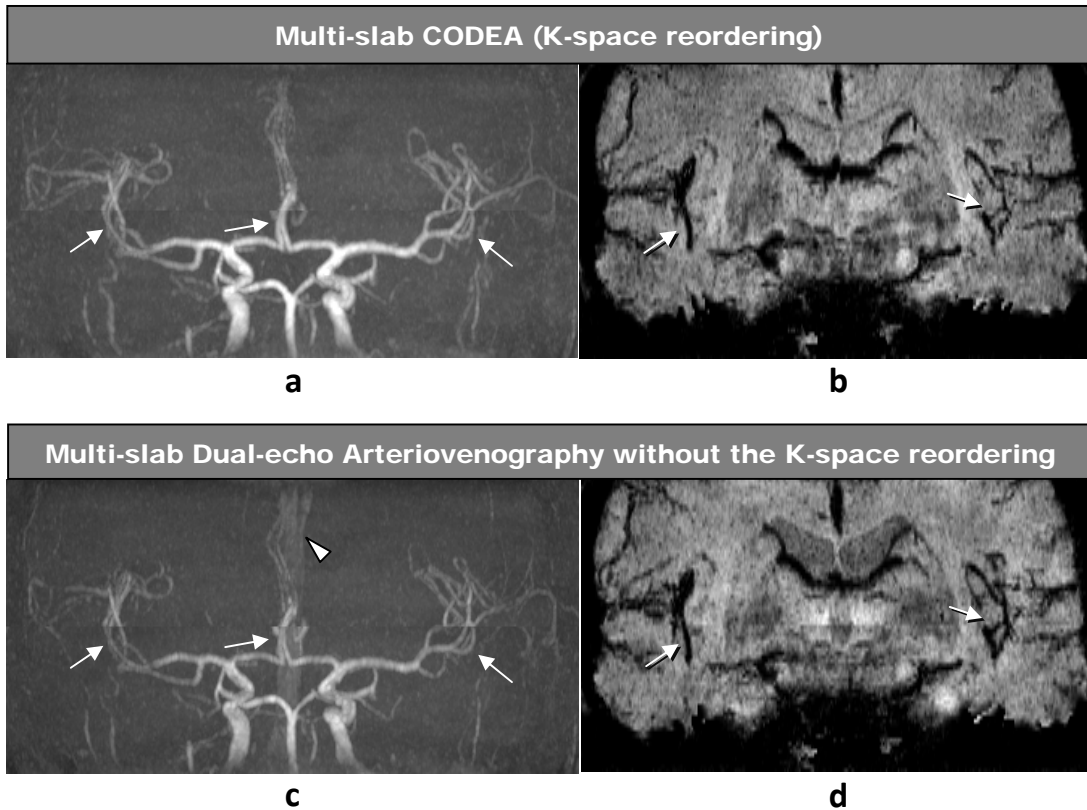


Figure 3.6 **Comparison of multi-slab CODEA MRA/MRV and multi-slab dual-echo MRA/MRV without K-space reordering scheme** in the same subject as Figures 3.4 and 3.5. **a** and **b**: TOF angiogram (**a**) and BOLD venogram (**b**) acquired using the CODEA with the echo-specific K-space reordering scheme. **c** and **d**: TOF angiogram (**c**) and BOLD venogram (**d**) acquired using the dual-echo angiography without K-space reordering (i.e., the conventional linearly-increasing k-space ordering was used in both echoes). An RF pulse with a flat excitation (flip angle 20°) was applied with no preparation pulse for the entire K-space regions in both echoes in **c** and **d**. Images in **a** and **c** are maximum-intensity projections over the entire 3D volume and images in **b** and **d** are minimum-intensity projections over a slab with 17-mm thickness. Scan resolution for all the angiograms is $0.43 \times 0.86 \times 1.4$ (mm^3). Because a flat excitation pulse was applied for both echoes in **c** and **d**, the venous signals were relatively uniform (arrows in **d**). On the other hand, discontinuities were apparent in the arterial signals around the overlapping regions of the slab (arrows in **c**), which can be ascribed to the downstream blood saturation effects. Uniform vascular contrast with no discontinuity was observed in the MRA and MRV in the multi-slab CODEA acquisition (arrows in **a** and **b**). The arrowhead in **c** indicates signals from a large vein.

3.4.3 Single-slab CODEA MRA/MRV with MTC pulse

The TR value was slightly lengthened when the MTC pulse was used (58 ms with vs 50 ms without the MTC). Nevertheless, the visualization of small arteries was improved with the MTC pulse for all tested subjects (Figure 3.7a and 7c). The tissue signal intensity in the CODEA MRA with the MTC pulse was reduced by $13 \pm 2\%$ compared to that without the MTC pulse, and the tissue SNR by $15 \pm 5\%$ (14.0 ± 1.8 with versus 16.5 ± 1.8 without MTC). On the other hand, the effect of the MTC on the CODEA MRV was negligible (Figure 3.7b and 7d): the tissue signal intensity increased by $4 \pm 5\%$ with the MTC pulse, and the tissue SNR by $2 \pm 7\%$ (21.4 ± 3.1 with versus 21.0 ± 2.9 without MTC). Note that tissue T_1 is 1–1.5 s at 3T (51) and that the tissue signal intensity is expected to increase by approximately 6% with the TR increase (from 50 to 58 ms) at the given flip angle (15°). This calculation along with our background tissue signal measurements again indicates that the MTC had little effect on the CODEA MRV.

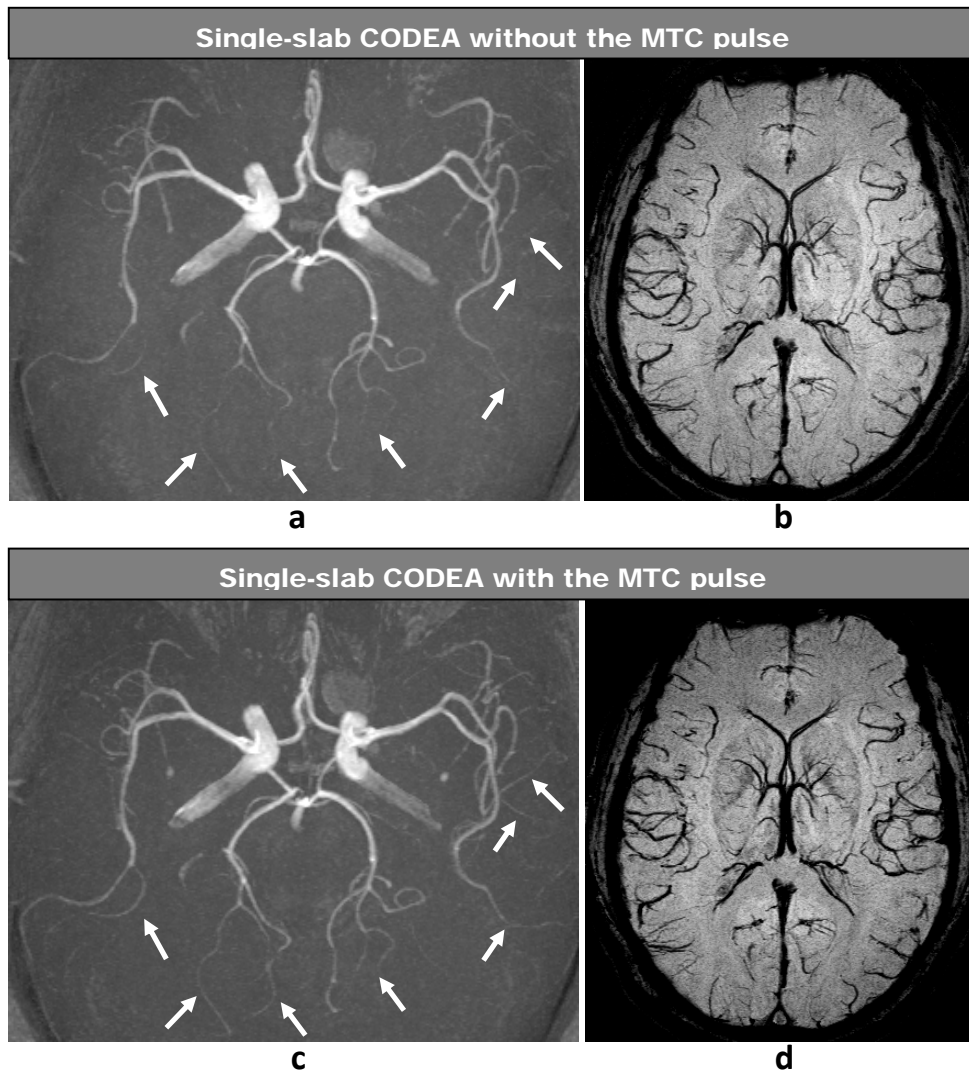


Figure 3.7 **Comparison of CODEA MRA/MRV without and with the MTC pulse** in a subject different from Figures 3.4–3.6. **a** and **b**: TOF angiogram (**a**) and BOLD venogram (**b**) acquired using the CODEA without the MTC pulse. **c** and **d**: TOF angiogram (**c**) and BOLD venogram (**d**) acquired using the CODEA with the MTC pulse. Images in **a** and **c** are maximum-intensity projections over the entire 3D volume, while images in **b** and **d** are minimum-intensity projections over a slab with 10-mm thickness. The MTC pulse improved the visualization of small vessels in TOF angiograms (arrows in **c**), with no apparent effect on the BOLD venogram (**d**).

3.5 DISCUSSION

In this study, we developed and tested an improved dual-echo arteriovenography technique (CODEA) which allowed us to acquire uniform and continuous 3D MRA images covering large brain volumes without degradation in the MRV image quality. Our preliminary results showed that the image quality and vascular contrast of the CODEA MRA/MRV were comparable to the individually-acquired conventional single-echo MRA and MRV. As a comparison, our implementation of a dual-echo arteriovenography with a flat RF pulse and no K-space reordering method demonstrated spatial signal intensity variations and vascular contrast reduction in the MRA. Continuous uniformity in the arterial signal intensity over a large brain volume is important for accurate assessment of the vascular integrity in brain imaging.

Maintaining a high SNR in the second echo (i.e. MRV) was challenging in the previous dual-echo technique (24), in part because both echoes (i.e., MRA and MRV) were acquired with the same parameters: acquisition bandwidth of 81 Hz/pixel, double slabs, and partial-echo sampling. In comparison, we used a lower acquisition bandwidth (34 Hz/pixel) in the second echo, which we estimated would improve the SNR by 54%. In the single-slab CODEA MRV, the SNR is expected to increase by $\sim 40\%$ (i.e., $\sqrt{2}$) compared to that in the double-slab acquisitions, while maintaining a good MRA vascular contrast and intensity uniformity. Furthermore, the use of the full-echo sampling for the second echo in the CODEA would contribute to the improvement in the SNR in the MRV.

Our preliminary results showed that techniques commonly used in conventional 3D TOF MR angiography such as MOTSA could be readily incorporated into the CODEA. However, any trade-off in the MRA/MRV vascular contrast that is associated with the number of the slabs cannot be resolved in the CODEA method.

In our study, the MTC pulse selectively suppressed the background tissue signal in the MRA, thus enhancing the arterial contrast (Figure 3.7c). On the other hand, the MTC had little effect on the venous contrast in the MRV (Figure 3.7d). A practical limitation of using MTC pulses in 3T MR angiography is that it increases the SAR. MTC pulse power has been reduced by weighting far more in the center than the periphery of the K-space regions (52,53). Although not tested in our study, a modified MTC could be incorporated into the CODEA to improve the arterial contrast without considerably increasing the SAR.

The comparison of the CODEA MRA and the conventional single-echo MRA demonstrated a slight contrast reduction in some small downstream arteries (Figure 3.4e). This is presumably due to the fact that the flip angle difference between the K-space center and edge regions was the highest in the downstream (Figure 3.1b). Small downstream arteries are more likely subjected to the changes in the characteristics of the K-space edge region (as well as the K-space center region) than large anatomical structures.

K-space reordering along only one not both PE directions is beneficial in that the un-reordered PE direction can be used to reduce scan time by means of the parallel imaging technique (54-56). On the other hand, K-space reordering along both PE directions has the potential to improve vascular contrast by means of increasing distance between the K-space center regions of the two echoes. One drawback of the reordering along both directions is the increased perturbations in the steady-state condition due to multiple transitions in the RF pulses. Further study is required to evaluate the effect of the different K-space reordering schemes on the echo-specific vascular contrast and its application to the optimization of the vascular contrast.

The proposed CODEA technique is likely useful for physiological studies and clinical diagnostic applications. An accurate assessment of some pathological conditions (e.g., Moyomoya disease (57), arterial venous malformation (58)) requires both arterial and venous vascular information. In a traditional contrast medium-enhanced angiography (X-ray or MR), the arteries and veins are distinguished because of their time-dependent dynamic contrast

enhancement and are displayed in a cine mode. When there are variations in the arteriovenous circulation paths or technical limitations in capturing the arteries or veins at specific scan time points, the arteries and veins may not be easily differentiable in a contrast-enhanced angiography. In contrast, with the CODEA technique, the arteries and veins are imaged at the same time (which is useful in minimizing temporal or physiological variation in imaging the vessels) and are identified for their distinct vascular contrast (dark and bright) in two different datasets.

4.0 APPLICATIONS OF BLOOD OXYGENATION LEVEL-DEPENDENT MICROSCOPY AND COMPATIBLE DUAL-ECHO ARTERIOVENOGRAPHY TO FUNCTIONAL AND CLINICAL STUDIES

4.1 IMPLICATIONS OF BOLD MRV FOR BOLD FMRI

4.1.1 Introduction

Blood oxygenation level-dependent (BOLD) functional MRI (fMRI) is a noninvasive tool for mapping brain function in various research fields including physiology, psychology, neuroscience, and pathology. Despite its ubiquitous usage, BOLD fMRI signals rely on secondary hemodynamic responses rather than primary neural activities. Accordingly, it has been reported that BOLD fMRI signals are correlated with large draining veins which may be far from neurons (28-31). However, correlation of BOLD fMRI maps with small intracortical venules has not been clear, and thus the spatial limitation of BOLD fMRI technique has been unclear. Since high-spatial resolution can now be achieved with BOLD fMRI in ultra high fields, comparison of the high-resolution BOLD fMRI maps with BOLD microscopic data will give insight into the spatial limitation of BOLD fMRI.

4.1.2 Methods

Three male Sprague-Dawley rats weighing 300–450 g were used with approval from the Institutional Animal Care and Use Committee (IACUC) at the University of Pittsburgh. The rats were initially anesthetized by inhalation of 5.0% isoflurane in a 7:3 mixture of N₂O:O₂ or N₂:O₂, and then intubated for mechanical ventilation (RSP-1002, Kent Scientific, CT, USA and SAR-830AP, CWE, PA, USA). The isoflurane level was reduced to 2.0% for surgical preparation. The femoral artery and femoral vein were catheterized for blood gas sampling and for administration of fluid, respectively. Then the N₂O:O₂ mixture was replaced with an air:O₂ mixture in a ratio to attain a fraction of inspired oxygen (FiO₂) of 30% and the isoflurane level was adjusted to ~1.5%. Rectal temperature was maintained at 37 ± 0.5 °C. Ventilation rate and volume were adjusted based on the blood gas analysis results (Stat profile pHox; Nova Biomedical, MA, USA and i-Stat, Fusoyakuhin, Japan) to maintain carbon dioxide partial pressure levels within 30–40 mm Hg. The head of the animal was carefully secured to a home-built cradle by means of ear pieces and a bite bar.

All experiments were carried out on a Varian 9.4 T / 31-cm MRI system (Palo Alto, CA) with an actively-shielded gradient coil of 12-cm inner diameter, which operates at a maximum gradient strength of 400 mT/m and a rise time of 130 μs. A home-built quadrature radiofrequency (RF) surface coil (inner diameter of each of 2 lobes = 1.6 cm) was positioned on top of the animal's head and provided RF excitation and reception. A 3D BOLD microscopic dataset was acquired with 3D RF-spoiled gradient-echo imaging. The RF power level was adjusted to maximize subcortical signal. Imaging parameters were: TR = 50 ms, TE = 20 ms, field of view = 3.0 × 1.5 × 1.5 cm³, corresponding matrix size = 384 × 192 × 192, voxel resolution = 78 μm (isotropic), number of averages = 2, and total scan time = 34.5 min. The largest field of view was along the readout direction (lateral-medial). Partial Fourier sampling (75%) was applied in both

phase-encode directions. Each 3D dataset was first zero-filled to a matrix size of $512 \times 256 \times 256$ and then Fourier-transformed to yield datasets with nominal isotropic voxel dimensions of $59 \mu\text{m}$.

For high-resolution fMRI studies, 2D gradient echo sequence with 1st order flow compensation along slice-select and readout directions was employed. Scan parameters were: TR = 20 ms, TE = 10 ms, FOV = 22×11 (mm²), Matrix = 256×128 , flip angle = 8° , thickness = 1 mm, and number of slices = 1. Each fMRI session was composed of a 38.4-s resting, a 15-s electrical stimulation, and a 61.8-s resting states (total 115.2 s), while the image acquisition was repeated 45 times per session. Electrical stimulation was applied to a forepaw with 3ms duration, 1.5 mA, and 6 Hz frequency. For each subject, 20–30 fMRI sessions were acquired repeatedly for averaging and there was at least 3-minute break between sessions for the recovery of hemodynamic response. Functional MRI maps were calculated as cross-correlation coefficient between MR signal and stimulation paradigm.

4.1.3 Results and Discussion

Functional MRI maps acquired with high-spatial resolution showed activation foci at the locations of intracortical veins (arrows in Figure 4.1) as well as large surface veins (arrowheads in Figure 4.1). The intracortical veins demonstrating correlation with the fMRI maps were relatively large in size and originated from deep cortical regions of depth around 1.2–1.7 mm, for all animals tested. The results imply that even if the spatial resolution of fMRI map increases, there is a limitation in mapping functional microarchitectures with the conventional gradient-echo (GE) based BOLD fMRI. Note that the density of the large intracortical veins detectable at the deep cortical regions (cortical depth of 1.6 mm) was ~ 1.5 vessels / mm² as demonstrated in the above Chapter II or Park et al (59). If we assume these intracortical venules are uniformly spaced, functional microarchitectures with spacing > 0.8 mm ($(1/1.5)^{1/2}$ mm) may be reasonably mapped with the conventional GE BOLD fMRI technique.

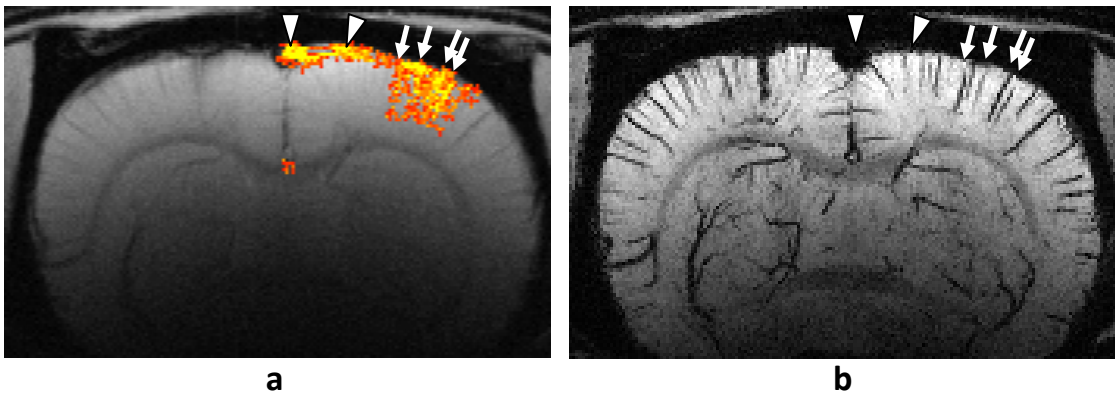


Figure 4.1 **Comparison of high-resolution BOLD fMRI map (a) and BOLD microscopic data (b).** Activation foci in the somatosensory cortex (a) are correlated with intracortical veins (b), as indicated by arrows, and some activation foci outside the somatosensory cortex (arrowheads) are located around regions of large draining veins including the superior sagittal sinus vein.

4.2 APPLICATIONS OF COMPATIBLE DUAL-ECHO ARTERIOVENOGRAPHY (CODEA) IN STROKE

4.2.1 Introduction

Clinical acute stroke requires rapid assessment of whether it is an ischemic or hemorrhagic stroke, the extent of infarction or irreversible damage representing the likelihood of hemorrhagic transformation, and the volume of penumbra, i.e. salvageable tissue, representing the potential for recovery with recanalization by thrombolysis or thrombectomy. The presence or absence and size of the penumbra vary substantially depending on the individual patients. Most patients with a large penumbra benefit by recanalization (60-62) whereas others may suffer hemorrhagic transformation with high morbidity and mortality (63). Hence, early and accurate assessment of the size of the penumbra and severity of the stroke is critical for ischemic stroke patients to get benefits from the only currently available treatment, namely, recanalization by thrombolysis or thrombolectomy.

In the clinical evaluation of acute stroke, x-ray computed tomography (CT) scans has been and continues to be the workhorse of emergency departments, because it is relatively lower in cost, quickly and easily detects blood structures, and does not require special screening. With the injection of contrast, CT angiography can be performed to define large vessel occlusions and also CT perfusion can be performed to get relative perfusion information which is especially useful for clinical stroke evaluation (64-66).

In a similar way to the CT study, MRI studies can be performed to assess infarction volume and existence of large vessel occlusion in ischemic stroke. Diffusion weighted imaging

(DWI) and perfusion weighted imaging (PWI) have been routinely tried for detection of ischemic penumbra (67). In addition to DWI and PWI, TOF MR angiography (MRA) has been also routinely performed for identification of arterial occlusion and recanalization after treatments.

For the appropriate assessment of hemorrhagic transformation, venous edematous status, blood clots, and venous shape and volume changes after onset of acute stroke, BOLD MR venography may also be an important imaging modality. Recently there have been limited trials of BOLD MR venography (MRV) (also known as susceptibility weighted imaging (6)) for acute stroke patients and one of the studies demonstrated detectability of hemorrhage more reliable than conventional CT method (68). Also, a preclinical study demonstrated that T_2^* -weighted imaging in combination with oxygen challenge may be used for accurate detection of ischemic penumbral regions (69). Nonetheless, BOLD MRV has been seldom performed in clinical acute stroke studies. One of the most important reasons would be that scan time allowed for acute stroke patients is extremely limited. By virtue of compatible dual-echo arteriovenography (CODEA) developed in this dissertation (Chapter III or Part et al (70)), however, we may be able to acquire the potentially valuable BOLD MRV with no additional examination time by simply replacing the conventional single-echo TOF MRA with CODEA.

In this section, CODEA was applied to *chronic* stroke patients who had experienced onset of acute stroke a few months before the study. These studies will give insight into the potential usefulness of the technique for *acute* stroke studies (within a few hours or days of onset of acute stroke).

4.2.2 Methods

All experiments were performed on a 3T whole-body scanner (Siemens Medical Solutions, Erlangen, Germany) with body coil transmission and 12-element head matrix coil reception. Three chronic stroke patients who experienced acute stroke a few months ago and provided

informed consent were scanned in this study approved by the Institutional Review Board. Voxel-localized shimming was performed with a vendor-supplied shim module based on a 3D phase map.

The pulse sequence diagram and the echo-specific K-space reordering scheme for CODEA acquisition are described in the previous chapter III. In brief, the first-order flow compensation was applied to both the slab-select and readout gradients. Imaging parameters were: time to repeat (TR) = 40 ms, TE = 3.2 / 20 ms, acquisition bandwidth = 150 / 50 Hz/pixel, matrix size = 512×192×64, corresponding field of view = 240×180×80 mm³, and number of averages = 1. A slice oversampling (20%) was employed to avoid a wrap-around artifact. The scan time for a 3D dataset was 9.8 min. A partial echo sampling (67%) was used in the first echo to reduce TE, while a full echo sampling in the second echo to improve SNR. The K-space center region in the first echo (TOF-weighted region, the first half of total data acquisition) was acquired with a ramped-profile RF excitation pulse with flip angle of 25° (20°–30°) and with a spatial presaturation pulse. The K-space center region in the second echo (BOLD-weighted region, the second half of total data acquisition) was acquired with a flat-profile RF excitation with flip angle of 15°. MTC pulse was not used so as to keep the specific absorption rate low.

Each 3D raw dataset was Fourier-transformed to generate 3D images with the matrix size of 512×384×170. The voxel dimensions became isotropic following a zero filling procedure. Venous contrast in MRV images was enhanced using phase-mask filtering (6). MRA images were displayed in maximum-intensity projections on the transaxial, sagittal, and coronal planes, whereas MRV images in minimum-intensity projections on the transaxial plane.

4.2.3 Results

One representative CODEA MRA/MRV images are shown in Figures 4.2 and 4.3. Detailed arterial vessels are detected in CODEA MRA including the occlusion of one of the two main arteries (Figure 4.2). Moreover, detailed veins were detected in the CODEA MRV (Figure 4.3). In some patients, hypointense structures not detectable in the normal hemisphere were observable in the contralateral hemisphere with arterial occlusion (arrow in Figure 4.3e). In some patients, venous structures detectable in normal hemisphere were not observable in the regions of arterial occlusion (data not shown). These changes in the venous structure in the regions of arterial occlusion were detectable in all the chronic stroke patients tested.

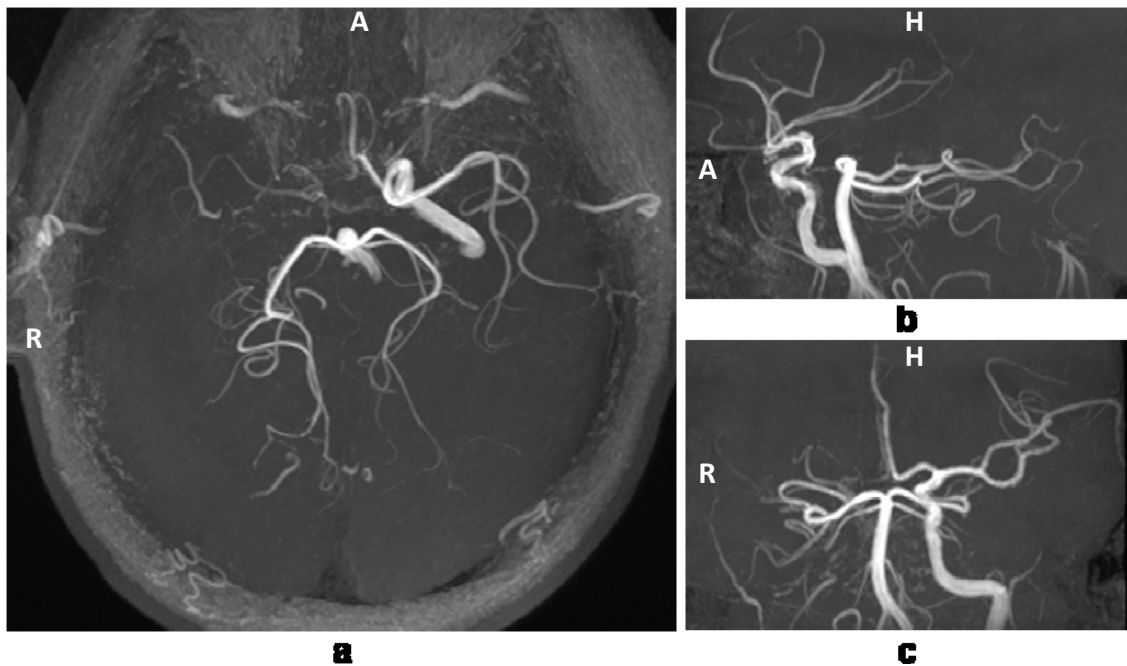


Figure 4.2 **A representative CODEA MRA in a stroke patient. (a)** Maximum-intensity projection image along axial direction overall entire brain region, **(b)** sagittal and **(c)** coronal maximum-intensity projection images of a brain region excluding the skull and subcutaneous tissue.

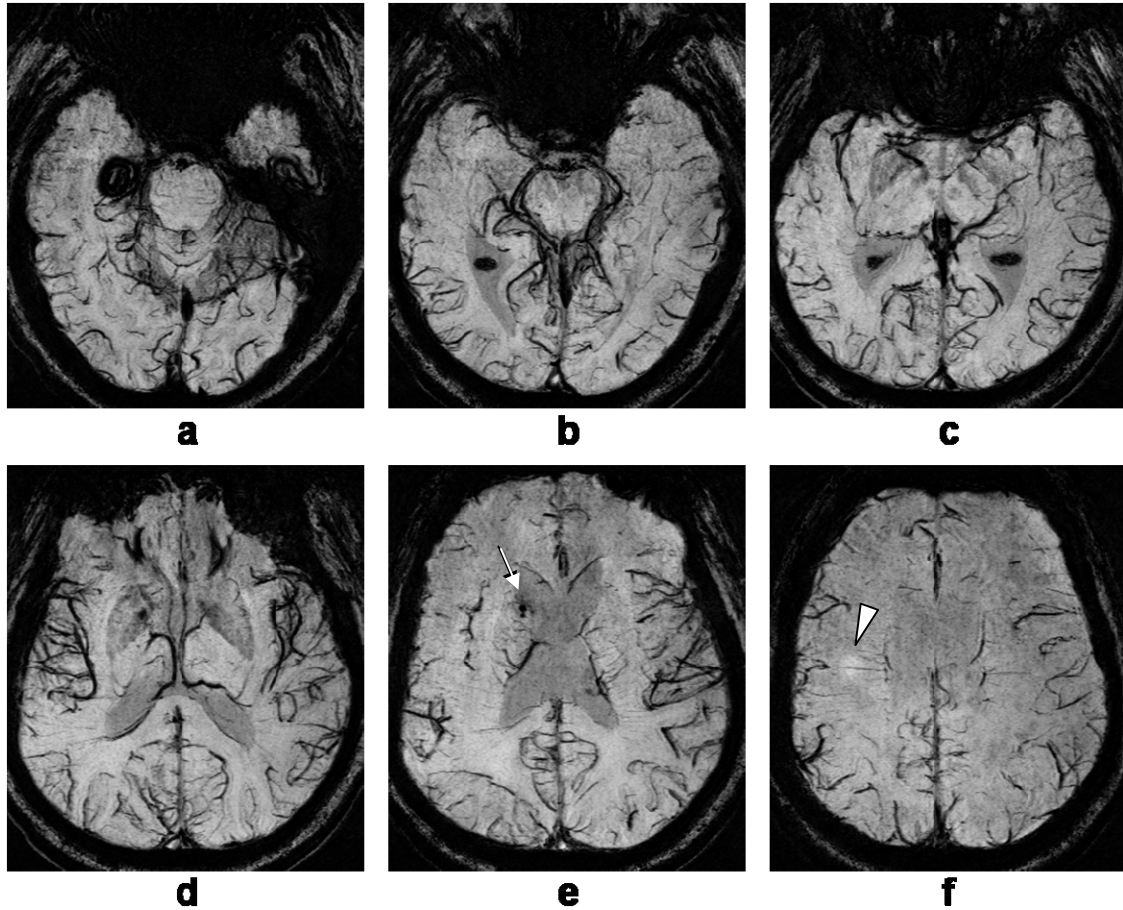


Figure 4.3 A representative CODEA MRV from the same subject as Figure 4.2. a-f: Minimum-intensity projection images at different locations over a thickness of 10 mm. The arrow in e represents a hypointense structure not detectable in the contralateral normal region. The arrowhead in f represents a site presumed to be infarction.

4.2.4 Discussion

CODEA MRA/MRV imaging was feasible for chronic stroke patients. Arterial occlusion and detailed venous structures were depicted in CODEA MRA/MRV. CODEA MRV was sensitive to changes in venous structures which might be ascribed to the onset of the arterial occlusion. Sensitivity of CODEA MRV to these structural changes in chronic stroke patients is in agreement with reliable detectability of hemorrhage using BOLD MRV in acute stroke patients observed in the previous study (68). Arterial and venous structures simultaneously detected with CODEA would be also useful for many other clinical studies.

In addition to visualization of blood vessels demonstrated in this study, BOLD MRV may provide more insights into imaging ischemic penumbra. DWI in combination with PWI (DWI/PWI mismatch) is being used to identify the ischemic penumbra, but can only achieve acceptable sensitivity and specificity levels with at least 260% mismatch (60). Nevertheless, the DWI/PWI mismatch is still clinically useful for assessment of the penumbral volume and potential of recovery with recanalization (60-62). This model was successful in part, but recent studies have reported that assessment of the ischemic penumbra by DWI and PWI mismatch is inaccurate, because DWI identifies infarct, penumbra, and even benign oligemia (71). Since these problems in the boundaries determined by DWI and PWI are likely related to the blood circulation around the region, BOLD MRV may give valuable information regarding the characteristics of these regions hence potential improvement in the identification of the penumbral region by modification of the mismatch region, because of its excellent small-vessel detectability. In particular, combination of cerebral blood flow (CBF) and cerebral blood volume (CBV) acquired with CT have been used by clinicians in assessing the presence of penumbra, demonstrating the importance of CBV information in stroke (72). However, CBV has been rarely quantified with MRI in stroke studies because of its difficulty in acquisition. As implicated from

the CT studies, segmented venous blood volume from CODEA MRV in combination with PWI may potentially improve the assessment of penumbral regions in acute stroke patients. Also, oxygen challenge in combination with BOLD MRV may be another approach for better identification of penumbral regions (69). By combining CODEA with CBF measured by contrast perfusion or arterial spin labeling (ASL), we may be able to accurately assess the penumbral and infarction volumes with MRI within 20 min. Ischemic penumbral regions were likely disappeared in the *chronic* stroke patients tested in this study, however it is worthwhile to apply BOLD MRV (hence CODEA) as well as DWI/PWI to *acute* stroke patients for better understanding of ischemic penumbral regions.

5.0 SUMMARY AND CONCLUSIONS

The detectability of intracortical vessels in BOLD MRV depends on a number of physiological and imaging parameters including vessel diameter, oxygenation, hematocrit level, magnetic field, TE, voxel resolution, and SNR. When BOLD MR venography was performed at 9.4T with TE = 20 ms and isotropic scan resolution = 78 μm , the diameter of the smallest-detectable venous vessels was in the range of ~16–30 μm for FiO_2 of ~30%, as demonstrated by our two-photon microscopy studies and computer simulations. Lower oxygenation levels improved the detectability of vessels, including those presumed to be arteries. Higher spatial resolution allowed the detection of even smaller vessels. This advancement of BOLD MR venography to BOLD microscopy by exploiting high-field advantages without exogenous contrast agent may provide valuable information for functional, developmental, and clinical studies of animals and humans.

We developed and tested a new dual-echo technique to simultaneously acquire both TOF MRA and BOLD MRV in a single acquisition at a clinical field of 3T. In this technique, the echo-specific K-space ordering scheme permitted the adjustment of the scan parameters compatible for both MRA and MRV. We demonstrated that the image quality in the MRA and MRV acquired by our compatible dual-echo arteriovenography (CODEA) technique was comparable to that for conventional single-echo MRA and MRV acquired in two different sessions. When our technique was integrated with MOTSA, seamless vascular connectivity was achieved in both MRA and MRV over a large coverage of the brain anatomy. Our technique would contribute to routine clinical acquisition and application of dual-echo MRA and MRV, as

both MRA and MRV can be acquired with minimal impact on the image quality and without adversely affecting the scan throughput.

As an application and extension of BOLD microscopy, the spatial limitation of conventional gradient-echo BOLD fMRI in a specific region was investigated. This was carried out by comparing high-resolution BOLD microscopic data and BOLD fMRI maps and evaluating the density of intracortical veins. As an application and extension of the CODEA technique, patients with chronic stroke were imaged using CODEA. Detailed arterial and venous structures including arterial occlusions and venous abnormalities were depicted. The CODEA technique appears useful to other clinical applications, particularly for those requiring efficient MRA/MRV imaging with limited scan time such as acute stroke studies.

APPENDIX A

COMPUTER SIMULATION STUDIES WITH A NUMERICAL SOLUTION OF BLOCH EQUATIONS FOR INVESTIGATION OF EXCITATION RF PULSE PROFILE USED IN TOF MR ANGIOGRAPHY AND COMPATIBLE DUAL-ECHO ARTERIOVENOGRAPHY (CODEA)

MR signals in the rotating frame can be expressed as Bloch equations as follows.

$$\frac{dM_{x'}}{dt} = -\Delta\omega \cdot M_{y'} - \gamma \cdot B_1(t)_{y'} \cdot M_z - \frac{M_{x'}}{T_2} \quad (3)$$

$$\frac{dM_{y'}}{dt} = \gamma \cdot B_1(t)_{x'} \cdot M_z + \Delta\omega \cdot M_{x'} - \frac{M_{y'}}{T_2} \quad (4)$$

$$\frac{dM_z}{dt} = \gamma \cdot B_1(t)_{y'} \cdot M_{x'} - \gamma \cdot B_1(t)_{x'} \cdot M_{y'} - \frac{M_0 - M_z}{T_1} \quad (5)$$

where $\Delta\omega$ represents frequency shift from the resonance frequency (i.e. $\Delta\omega = \omega - \omega_0$), $B_1(t)_{x'}$ and $B_1(t)_{y'}$ real and imaginary RF pulse signals. For simplicity, denote the above equations 3-5 as

$$\left[\frac{dM_x}{dt} \quad \frac{dM_y}{dt} \quad \frac{dM_z}{dt} \right]^T = f(t, [M_x \quad M_y \quad M_z]^T) \quad (6)$$

In this dissertation, the above Bloch equations were solved with embedded Runge-Kutta method (50) as follows.

$$k_1 = h \cdot f(t_n, [M_x \ M_y \ M_z]_n^T) \quad (7)$$

$$k_2 = h \cdot f(t_n + a_2 \cdot h, [M_x \ M_y \ M_z]_n^T + b_{21} \cdot k_1) \quad (8)$$

$$k_3 = h \cdot f(t_n + a_3 \cdot h, [M_x \ M_y \ M_z]_n^T + b_{31} \cdot k_1 + b_{32} \cdot k_2) \quad (9)$$

$$k_4 = h \cdot f(t_n + a_4 \cdot h, [M_x \ M_y \ M_z]_n^T + b_{41} \cdot k_1 + b_{42} \cdot k_2 + b_{43} \cdot k_3) \quad (10)$$

$$k_5 = h \cdot f(t_n + a_5 \cdot h, [M_x \ M_y \ M_z]_n^T + b_{51} \cdot k_1 + b_{52} \cdot k_2 + b_{53} \cdot k_3 + b_{54} \cdot k_4) \quad (11)$$

$$k_6 = h \cdot f(t_n + a_6 \cdot h, [M_x \ M_y \ M_z]_n^T + b_{61} \cdot k_1 + b_{62} \cdot k_2 + b_{63} \cdot k_3 + b_{64} \cdot k_4 + b_{65} \cdot k_5) \quad (12)$$

where $[M_x \ M_y \ M_z]_n^T$ denotes magnetizations at the time point of t_n and the coefficient values are

$$[a_2 \ a_3 \ a_4 \ a_5 \ a_6] = [1/5 \ 3/10 \ 3/5 \ 1 \ 7/8] \quad (13)$$

$$[b_{21}] = [1/5] \quad (14)$$

$$[b_{31} \ b_{32}] = [3/40 \ 9/40] \quad (15)$$

$$[b_{41} \ b_{42} \ b_{43}] = [3/10 \ -9/10 \ 6/5] \quad (16)$$

$$[b_{51} \ b_{52} \ b_{53} \ b_{54}] = [-11/54 \ 5/2 \ -70/27 \ 35/27] \quad (17)$$

$$[b_{61} \ b_{62} \ b_{63} \ b_{64} \ b_{65}] = \left[\frac{1631}{55296} \ \frac{175}{512} \ \frac{575}{13824} \ \frac{44275}{110592} \ \frac{253}{4096} \right] \quad (18)$$

$$[c_1 \ c_2 \ c_3 \ c_4 \ c_5 \ c_6] = \left[\frac{2825}{27648} \ 0 \ \frac{18575}{48384} \ \frac{13525}{55296} \ \frac{277}{14336} \ \frac{1}{4} \right] \quad (19)$$

Assume initial magnetization to be $M = [M_x \ M_y \ M_z]_0^T = [0 \ 0 \ 1]^T$, then the magnetization at the new time point t_{n+1} can be recursively calculated from the given magnetization at the current time point of t_n as follows.

$$[M_x \ M_y \ M_z]_{n+1}^T = [M_x \ M_y \ M_z]_n^T + c_1 \cdot k_1 + c_2 \cdot k_2 + c_3 \cdot k_3 + c_4 \cdot k_4 + c_5 \cdot k_5 \quad (20)$$

Since RF pulse duration is usually much shorter than T_1 and T_2 of tissue of interest, the last terms in the above equations 3–5 which include T_1 and T_2 was ignored in the calculation of RF pulse excitation profile in the main body of the dissertation.

APPENDIX B

COMPUTER SIMULATION STUDIES WITH TWO-COMPARTMENT MODEL FOR EXAMINATION OF DETECTABILITY OF 9.4T BOLD MICROSCOPY

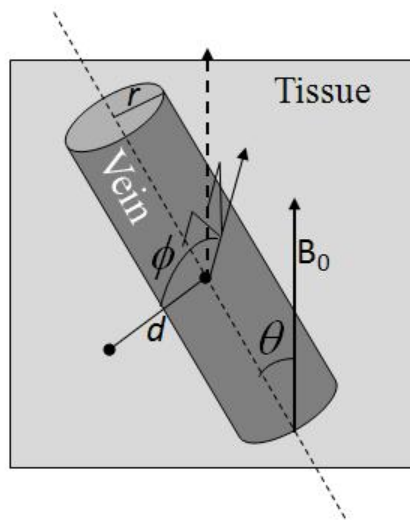


Figure 5.1 **Two compartment model of a vein and surrounding tissue.** Please see the text for details.

Phase and magnitude signals inside and outside a blood vessel surrounded by tissue can be calculated based on the infinitely long cylinder model (18,20,21,42) and

steady state signal intensity of GRE sequence. The phase of intra- and extra-vascular spins can be described as

$$\Delta\phi_{in} = -\gamma \cdot \frac{\Delta\chi}{2} \cdot \left(\cos^2 \theta - \frac{1}{3} \right) \cdot B_0 \cdot TE \quad (21)$$

$$\Delta\phi_{ex} = -\gamma \cdot \left(\frac{\Delta\chi}{2} \cdot \sin^2 \theta \cdot \frac{r^2}{d^2} \cdot \cos 2\phi \right) \cdot B_0 \cdot TE \quad (22)$$

where θ is the angle between the blood vessel and main magnetic field, r is the radius of the blood vessel, d is the distance between a point of interest outside the vein and the center of the blood vessel, ϕ is the angle between d and the plane defined by the main magnetic field and the blood vessel, $\Delta\chi$ is the susceptibility difference between the blood vessel and tissue which is given as

$$\Delta\chi = 4 \cdot \pi \cdot \Delta\chi_0 \cdot Hct \cdot (1 - Y) \quad (23)$$

$\Delta\chi_0$ is the susceptibility difference between completely deoxygenated and completely oxygenated red blood cells, and Hct is the hematocrit level of the venous blood. And the magnitude of intra- and extra-vascular spins can be described as

$$S_{in} = \rho_v \cdot \frac{(1 - \exp(-TR/T_{1v})) \cdot \sin(\alpha)}{(1 - \cos(\alpha) \cdot \exp(-TR/T_{1v}))} \cdot \exp(-TE/T_{2v}) \quad (24)$$

$$S_{ex} = \rho_t \cdot \frac{(1 - \exp(-TR/T_{1t})) \cdot \sin(\alpha)}{(1 - \cos(\alpha) \cdot \exp(-TR/T_{1t}))} \cdot \exp(-TE/T_{2t}) \quad (25)$$

where ρ_v and ρ_t are spin densities of venous blood and tissue respectively, T_{1v} and T_{1t} are longitudinal relaxation times of venous blood and tissue respectively, T_{2v} and T_{2t} are transverse relaxation times of venous blood and tissue respectively, and α is the flip angle. Here, T_2 values (rather than T_2^* values) are used in the equations (24) and (25), because the B_0 inhomogeneity induced by the susceptibility of the blood vessel can be taken into account when pixel signals are integrated and the local background inhomogeneity is assumed to be negligible within this small region of interest. Assuming a hematocrit level of 0.4 and the susceptibility difference between 100% oxyhemoglobin and 100% dHb of 0.2 ppm (21), $\Delta\chi_0$ in whole blood is 0.08 ppm.

MR signals are integration of all the spins within a pixel, therefore pixel gridding position greatly affects the MR pixel signal intensity. Under the assumption that blood vessels are infinitely long compared to pixel size, we can reconstruct the MR pixels in a 2D plane perpendicular to a blood vessel of interest rather than a 3D VOI to minimize calculation amount. Then, with given scan resolution, the MR pixel signals are a function of spatial gridding position, which can be considered in a 2D plane. Distortion effect of a spin is ignored in this simulation of venous detectability. The final MR complex pixel signals are calculated as a sum of all the sub-points determined by the finite-difference method (e.g. element width of 1/10 of the pixel width), as a function of 4 variables, Y , r , the 2D spatial gridding position.

$$S = \sum_{n=1}^N S_n \exp(i \cdot \phi_n) \quad (26)$$

where N is total number of sub-points within each pixel (100 in this case), S_n and ϕ_n are magnitude and phase signals at each sub-point determined by the above equations 21, 22, 24, and 25, and i is square root of -1.

APPENDIX C

CONTRIBUTORS TO THE WORKS

1.0 INTRODUCTION

Sung-Hong Park^{1,2} and Kyongtae Ty Bae^{1,2}

¹Department of Bioengineering, University of Pittsburgh, Pittsburgh, Pennsylvania

²Department of Radiology, University of Pittsburgh, Pittsburgh, Pennsylvania

2.0 IMAGING BRAIN VASCULATURE WITH BLOOD OXYGENATION LEVEL-DEPENDENT MICROSCOPY: MR DETECTION LIMITS DETERMINED BY IN VIVO TWO-PHOTON MICROSCOPY

- (i) Demonstration of the prototype MR images and initiation of the project
Sung-Hong Park
- (ii) Development of ideas regarding the TE-dependent studies and the computer simulations
Sung-Hong Park
- (iii) Development of ideas regarding the oxygenation-dependent studies, blood vessel counting, and two-photon microscopy studies
Seong-Gi Kim
- (iv) Experimental design
Sung-Hong Park and Seong-Gi Kim

- (v) All the pulse sequence programming, data acquisition, processing, quantification, and analysis in terms of MR studies
Sung-Hong Park
 - (vi) All data acquisition, processing, and quantification in terms of the two-photon microscopy studies
Kazuto Masamoto
 - (vii) Paper writing and publication
Sung-Hong Park^{1,2}, Kazuto Masamoto³, Kristy Hendrich², Iwao Kanno³, and Seong-Gi Kim^{2,4}
- ¹Department of Bioengineering, University of Pittsburgh, Pittsburgh, Pennsylvania
²Department of Radiology, University of Pittsburgh, Pittsburgh, Pennsylvania
³Molecular Imaging Center, National Institute of Radiological Sciences, Chiba, Japan
⁴Department of Neurobiology, University of Pittsburgh, Pittsburgh, Pennsylvania

3.0 COMPATIBLE DUAL-ECHO ARTERIOVENOGRAPHY (CODEA) USING AN ECHO-SPECIFIC K-SPACE REORDERING SCHEME BASED ON TIME-OF-FLIGHT (TOF) AND BLOOD OXYGENATION LEVEL-DEPENDENT (BOLD) EFFECTS

- (i) Invention of the idea and initiation of the project
Sung-Hong Park and Kyongtae Ty Bae
 - (ii) Experimental design
Sung-Hong Park and Kyongtae Ty Bae
 - (iii) All the pulse sequence programming, data acquisition, processing, and analysis
Sung-Hong Park
 - (iv) Paper writing and publication
Sung-Hong Park^{1,2}, Chan-Hong Moon², and Kyongtae Ty Bae^{1,2}
- ¹Department of Bioengineering, University of Pittsburgh, Pittsburgh, Pennsylvania
²Department of Radiology, University of Pittsburgh, Pittsburgh, Pennsylvania

4.0 APPLICATIONS OF BLOOD OXYGENATION LEVEL-DEPENDENT MICROSCOPY AND COMPATIBLE DUAL-ECHO ARTERIOVENOGRAPHY TO FUNCTIONAL AND CLINICAL STUDIES

4.1 IMPLICATIONS OF BOLD MRV FOR BOLD FMRI

- (i) Initiation of the project
Seong-Gi Kim and Sung-Hong Park
- (ii) All the pulse sequence programming, data acquisition, processing, and analysis
Sung-Hong Park
- (iii) Chapter writing
Sung-Hong Park^{1,2}, Seong-Gi Kim^{1,3}, and Kyongtae Ty Bae^{1,2}
¹Department of Bioengineering, University of Pittsburgh, Pittsburgh, Pennsylvania
²Department of Radiology, University of Pittsburgh, Pittsburgh, Pennsylvania
³Department of Neurobiology, University of Pittsburgh, Pittsburgh, Pennsylvania

4.2 APPLICATIONS OF COMPATIBLE DUAL-ECHO ARTERIOVENOGRAPHY (CODEA) IN STROKE

- (i) Idea development
Kyongtae Ty Bae, Edwin Nemoto, and Sung-Hong Park
- (ii) Pulse sequence programming and data processing
Sung-Hong Park
- (iii) Chapter writing
Sung-Hong Park^{1,2}, Edwin Nemoto², and Kyongtae Ty Bae^{1,2}
¹Department of Bioengineering, University of Pittsburgh, Pittsburgh, Pennsylvania
²Department of Radiology, University of Pittsburgh, Pittsburgh, Pennsylvania

5.0 SUMMARY AND CONCLUSIONS

Sung-Hong Park^{1,2} and Kyongtae Ty Bae^{1,2}

¹Department of Bioengineering, University of Pittsburgh, Pittsburgh, Pennsylvania

²Department of Radiology, University of Pittsburgh, Pittsburgh, Pennsylvania

APPENDIX A. COMPUTER SIMULATION STUDIES WITH A NUMERICAL SOLUTION OF BLOCH EQUATIONS FOR INVESTIGATION OF EXCITATION RF PULSE PROFILE USED IN TOF MR ANGIOGRAPHY AND COMPATIBLE DUAL-ECHO ARTERIOVENOGRAPHY (CODEA)

Sung-Hong Park

APPENDIX B. COMPUTER SIMULATION STUDIES WITH TWO-COMPARTMENT MODEL FOR EXAMINATION OF DETECTABILITY OF 9.4T BOLD MICROSCOPY

Sung-Hong Park

BIBLIOGRAPHY

1. Lauenstein TC, Salman K, Morreira R, Tata S, Tudorascu D, Baramidze G, Singh-Parker S, Martin DR. Nephrogenic systemic fibrosis: center case review. *J Magn Reson Imaging* 2007;26(5):1198-1203.
2. Dumoulin CL, Hart HR, Jr. Magnetic resonance angiography in the head and neck. *Acta Radiol Suppl* 1986;369:17-20.
3. Dumoulin CL, Souza SP, Walker MF, Wagle W. Three-dimensional phase contrast angiography. *Magn Reson Med* 1989;9(1):139-149.
4. Ogawa S, Lee TM. Magnetic resonance imaging of blood vessels at high fields: in vivo and in vitro measurements and image simulation. *Magn Reson Med* 1990;16(1):9-18.
5. Ogawa S, Lee TM, Nayak AS, Glynn P. Oxygenation-sensitive contrast in magnetic resonance image of rodent brain at high magnetic fields. *Magn Reson Med* 1990;14(1):68-78.
6. Haacke EM, Xu Y, Cheng YC, Reichenbach JR. Susceptibility weighted imaging (SWI). *Magn Reson Med* 2004;52(3):612-618.
7. Reichenbach JR, Venkatesan R, Schillinger DJ, Kido DK, Haacke EM. Small vessels in the human brain: MR venography with deoxyhemoglobin as an intrinsic contrast agent. *Radiology* 1997;204(1):272-277.
8. Wehrli FW, Shimakawa A, Gullberg GT, MacFall JR. Time-of-flight MR flow imaging: selective saturation recovery with gradient refocusing. *Radiology* 1986;160(3):781-785.
9. Atkinson D, Brant-Zawadzki M, Gillan G, Purdy D, Laub G. Improved MR angiography: magnetization transfer suppression with variable flip angle excitation and increased resolution. *Radiology* 1994;190(3):890-894.
10. Nagele T, Klose U, Grodd W, Petersen D, Tintera J. The effects of linearly increasing flip angles on 3D inflow MR angiography. *Magn Reson Med* 1994;31(5):561-566.

11. Pauly J, Roux PL, Nishimura D, Macovski A. Parameter Relations for the Shinnar-Le Roux Selective Excitation Pulse Design Algorithm. *IEEE Trans Med Imaging* 1991;10(1):53-65.
12. Haacke EM, Brown RW, Thompson MR, Venkatesan R. SNR dependence on imaging parameters. In: Haacke EM, Brown RW, Thompson MR, Venkatesan R, editors *Magnetic resonance imaging, physical principles and sequence design* New York: John Wiley & Sons, Inc 1999:p340-349.
13. Parker DL, Yuan C, Blatter DD. MR angiography by multiple thin slab 3D acquisition. *Magn Reson Med* 1991;17(2):434-451.
14. Edelman RR, Ahn SS, Chien D, Li W, Goldmann A, Mantello M, Kramer J, Kleefield J. Improved time-of-flight MR angiography of the brain with magnetization transfer contrast. *Radiology* 1992;184(2):395-399.
15. Pike GB, Hu BS, Glover GH, Enzmann DR. Magnetization transfer time-of-flight magnetic resonance angiography. *Magn Reson Med* 1992;25(2):372-379.
16. Blatter DD, Parker DL, Robison RO. Cerebral MR angiography with multiple overlapping thin slab acquisition. Part I. Quantitative analysis of vessel visibility. *Radiology* 1991;179(3):805-811.
17. Du YP, Parker DL, Davis WL, Cao G. Reduction of partial-volume artifacts with zero-filled interpolation in three-dimensional MR angiography. *J Magn Reson Imaging* 1994;4(5):733-741.
18. Reichenbach JR, Haacke EM. High-resolution BOLD venographic imaging: a window into brain function. *NMR Biomed* 2001;14(7-8):453-467.
19. Wang Y, Yu Y, Li D, Bae KT, Brown JJ, Lin W, Haacke EM. Artery and vein separation using susceptibility-dependent phase in contrast-enhanced MRA. *J Magn Reson Imaging* 2000;12(5):661-670.
20. Xu Y, Haacke EM. The role of voxel aspect ratio in determining apparent vascular phase behavior in susceptibility weighted imaging. *Magn Reson Imaging* 2006;24(2):155-160.
21. Weisskoff RM, Kiihne S. MRI susceptometry: image-based measurement of absolute susceptibility of MR contrast agents and human blood. *Magn Reson Med* 1992;24(2):375-383.
22. Lee SP, Silva AC, Ugurbil K, Kim SG. Diffusion-weighted spin-echo fMRI at 9.4 T: microvascular/tissue contribution to BOLD signal changes. *Magn Reson Med* 1999;42(5):919-928.

23. Spees W, Yablonskiy D, Oswood M, Ackerman JH. Water Proton MR Properties of Human Blood at 1.5 Tesla: Magnetic Susceptibility, T1, T2, T*2, and Non-Lorentzian Signal Behavior. *Magn Reson Med* 2001;45:533-542.
24. Du YP, Jin Z. Simultaneous acquisition of MR angiography and venography (MRAV). *Magn Reson Med* 2008;59(5):954-958.
25. Ogawa S, Tank DW, Menon R, Ellermann JM, Kim S-G, Merkle H, Ugurbil K. Intrinsic Signal Changes Accompanying Sensory Stimulation: Functional Brain Mapping with Magnetic Resonance Imaging. *Proc Natl Acad Sci USA* 1992;89:5951-5955.
26. Bandettini PA, Wong EC, Hinks RS, Tikofsky RS, Hyde JS. Time course EPI of human brain function during task activation. *Magn Reson Med* 1992;25(2):390-397.
27. Kwong KK, Belliveau JW, Chesler DA, Goldberg IE, Weisskoff RM, Poncelet BP, Kennedy DN, Hoppel BE, Cohen MS, Turner R, et al. Dynamic magnetic resonance imaging of human brain activity during primary sensory stimulation. *Proc Natl Acad Sci U S A* 1992;89(12):5675-5679.
28. Hoogenraad FG, Pouwels PJ, Hofman MB, Reichenbach JR, Sprenger M, Haacke EM. Quantitative differentiation between BOLD models in fMRI. *Magn Reson Med* 2001;45(2):233-246.
29. Kim SG, Hendrich K, Hu X, Merkle H, Ugurbil K. Potential pitfalls of functional MRI using conventional gradient-recalled echo techniques. *NMR Biomed* 1994;7(1-2):69-74.
30. Krings T, Erberich SG, Roessler F, Reul J, Thron A. MR blood oxygenation level-dependent signal differences in parenchymal and large draining vessels: implications for functional MR imaging. *AJNR Am J Neuroradiol* 1999;20(10):1907-1914.
31. Lai S, Hopkins AL, Haacke EM, Li D, Wasserman BA, Buckley P, Friedman L, Meltzer H, Hedera P, Friedland R. Identification of vascular structures as a major source of signal contrast in high resolution 2D and 3D functional activation imaging of the motor cortex at 1.5T: preliminary results. *Magn Reson Med* 1993;30(3):387-392.
32. Bolan PJ, Yacoub E, Garwood M, Ugurbil K, Harel N. In vivo micro-MRI of intracortical neurovasculature. *Neuroimage* 2006;32(1):62-69.
33. Christoforidis GA, Bourekas EC, Baujan M, Abduljalil AM, Kangarlu A, Spigos DG, Chakeres DW, Robitaille PM. High resolution MRI of the deep brain vascular anatomy at 8 Tesla: susceptibility-based enhancement of the venous structures. *J Comput Assist Tomogr* 1999;23(6):857-866.
34. Kleinfeld D, Mitra PP, Helmchen F, Denk W. Fluctuations and stimulus-induced changes in blood flow observed in individual capillaries in layers 2 through 4 of the rat neocortex. *Proc Nat Acad Sci* 1998;95:15741-15746.

35. Gray LH, Steadman JM. Determination of the Oxyhaemoglobin Dissociation Curves for Mouse and Rat Blood. *J Physiol* 1964;175:161-171.
36. Bottomley PA. Spatial localization in NMR spectroscopy in vivo. *Ann N Y Acad Sci* 1987;508:333-348.
37. Cohen MS, DuBois RM, Zeineh MM. Rapid and effective correction of RF inhomogeneity for high field magnetic resonance imaging. *Hum Brain Mapp* 2000;10(4):204-211.
38. Gudbjartsson H, Patz S. The Rician distribution of noisy MRI data. *Magn Reson Med* 1995;34(6):910-914.
39. Paxinos G, Watson C. *The rat brain in stereotaxic coordinates*. San Diego: Academic Press; 1986.
40. Rose A. The sensitivity performance of the human eye on an absolute scale. *J Opt Soc Am* 1948;38:196-208.
41. Vovenko E. Distribution of oxygen tension on the surface of arterioles, capillaries and venules of brain cortex and in tissue in normoxia: an experimental study on rats. *Pflugers Arch* 1999;437(4):617-623.
42. Ogawa S, Menon RS, Tank DW, Kim S-G, Merkle H, Ellermann JM, Ugurbil K. Functional Brain Mapping by Blood Oxygenation Level-Dependent Contrast Magnetic Resonance Imaging. *Biophys J* 1993;64:800-812.
43. Tsekos NV, Zhang F, Merkle H, Nagayama M, Iadecola C, Kim SG. Quantitative measurements of cerebral blood flow in rats using the FAIR technique: correlation with previous iodoantipyrine autoradiographic studies. *Magn Reson Med* 1998;39(4):564-573.
44. Silvennoinen MJ, Clingman CS, Golay X, Kauppinen RA, van Zijl PC. Comparison of the dependence of blood R2 and R2* on oxygen saturation at 1.5 and 4.7 Tesla. *Magn Reson Med* 2003;49(1):47-60.
45. Kennan RP, Zhong J, Gore JC. Intravascular susceptibility contrast mechanisms in tissues. *Magn Reson Med* 1994;31:9-21.
46. Lee BC, Vo KD, Kido DK, Mukherjee P, Reichenbach J, Lin W, Yoon MS, Haacke M. MR high-resolution blood oxygenation level-dependent venography of occult (low-flow) vascular lesions. *AJNR Am J Neuroradiol* 1999;20(7):1239-1242.
47. Sehgal V, Delproposito Z, Haacke EM, Tong KA, Wycliffe N, Kido DK, Xu Y, Neelavalli J, Haddar D, Reichenbach JR. Clinical applications of neuroimaging with susceptibility-weighted imaging. *J Magn Reson Imaging* 2005;22(4):439-450.

48. Tan IL, van Schijndel RA, Pouwels PJ, van Walderveen MA, Reichenbach JR, Manoliu RA, Barkhof F. MR venography of multiple sclerosis. *AJNR Am J Neuroradiol* 2000;21(6):1039-1042.
49. Barnes S, Manova E, Haacke EM. Angiography and Venography in a Single SWI Acquisition. *Proc Intl Soc Magn Reson Med* 2008;16:2231.
50. Cash JR, Karp AH. A variable order Runge-Kutta method for initial value problems with rapidly varying right-hand sides. *ACM Transactions on Mathematical Software* 1990;16(3):201-222.
51. Ethofer T, Mader I, Seeger U, Helms G, Erb M, Grodd W, Ludolph A, Klose U. Comparison of longitudinal metabolite relaxation times in different regions of the human brain at 1.5 and 3 Tesla. *Magn Reson Med* 2003;50(6):1296-1301.
52. Lin C, Bernstein MA, Gibbs GF, Huston J, 3rd. Reduction of RF power for magnetization transfer with optimized application of RF pulses in k-space. *Magn Reson Med* 2003;50(1):114-121.
53. Parker DL, Buswell HR, Goodrich KC, Alexander AL, Keck N, Tsuruda JS. The application of magnetization transfer to MR angiography with reduced total power. *Magn Reson Med* 1995;34(2):283-286.
54. Griswold MA, Jakob PM, Heidemann RM, Nittka M, Jellus V, Wang J, Kiefer B, Haase A. Generalized autocalibrating partially parallel acquisitions (GRAPPA). *Magn Reson Med* 2002;47(6):1202-1210.
55. Pruessmann KP, Weiger M, Scheidegger MB, Boesiger P. SENSE: sensitivity encoding for fast MRI. *Magn Reson Med* 1999;42(5):952-962.
56. Sodickson DK, Manning WJ. Simultaneous acquisition of spatial harmonics (SMASH): fast imaging with radiofrequency coil arrays. *Magn Reson Med* 1997;38(4):591-603.
57. Fushimi Y, Miki Y, Kikuta K, Okada T, Kanagaki M, Yamamoto A, Nozaki K, Hashimoto N, Hanakawa T, Fukuyama H, Togashi K. Comparison of 3.0- and 1.5-T three-dimensional time-of-flight MR angiography in moyamoya disease: preliminary experience. *Radiology* 2006;239(1):232-237.
58. Hadizadeh DR, von Falkenhausen M, Gieseke J, Meyer B, Urbach H, Hoogeveen R, Schild HH, Willinek WA. Cerebral arteriovenous malformation: Spetzler-Martin classification at subsecond-temporal-resolution four-dimensional MR angiography compared with that at DSA. *Radiology* 2008;246(1):205-213.
59. Park SH, Masamoto K, Hendrich K, Kanno I, Kim SG. Imaging brain vasculature with BOLD microscopy: MR detection limits determined by in vivo two-photon microscopy. *Magn Reson Med* 2008;59(4):855-865.

60. Kakuda W, Lansberg MG, Thijs VN, Kemp SM, Bammer R, Wechsler LR, Moseley ME, Marks MP, Albers GW. Optimal definition for PWI/DWI mismatch in acute ischemic stroke patients. *J Cereb Blood Flow Metab* 2008;28(5):887-891.
61. Kakuda W, Hamilton S, Thijs VN, Lansberg MG, Kemp S, Skalabrin E, Albers GW. Optimal outcome measures for detecting clinical benefits of early reperfusion: insights from the DEFUSE Study. *J Stroke Cerebrovasc Dis* 2008;17(4):235-240.
62. Furlan AJ, Eyding D, Albers GW, Al-Rawi Y, Lees KR, Rowley HA, Sachara C, Soehngen M, Warach S, Hacke W. Dose Escalation of Desmoteplase for Acute Ischemic Stroke (DEDAS): evidence of safety and efficacy 3 to 9 hours after stroke onset. *Stroke* 2006;37(5):1227-1231.
63. Adams HP, Jr., del Zoppo G, Alberts MJ, Bhatt DL, Brass L, Furlan A, Grubb RL, Higashida RT, Jauch EC, Kidwell C, Lyden PD, Morgenstern LB, Qureshi AI, Rosenwasser RH, Scott PA, Wijndicks EF. Guidelines for the early management of adults with ischemic stroke: a guideline from the American Heart Association/American Stroke Association Stroke Council, Clinical Cardiology Council, Cardiovascular Radiology and Intervention Council, and the Atherosclerotic Peripheral Vascular Disease and Quality of Care Outcomes in Research Interdisciplinary Working Groups: The American Academy of Neurology affirms the value of this guideline as an educational tool for neurologists. *Circulation* 2007;115(20):e478-534.
64. Cianfoni A, Colosimo C, Basile M, Wintermark M, Bonomo L. Brain perfusion CT: principles, technique and clinical applications. *Radiol Med* 2007;112(8):1225-1243.
65. Provenzale JM, Wintermark M. Optimization of perfusion imaging for acute cerebral ischemia: review of recent clinical trials and recommendations for future studies. *AJR Am J Roentgenol* 2008;191(4):1263-1270.
66. Wintermark M, Sincic R, Sridhar D, Chien JD. Cerebral perfusion CT: technique and clinical applications. *J Neuroradiol* 2008;35(5):253-260.
67. Schlaug G, Benfield A, Baird AE, Siewert B, Lovblad KO, Parker RA, Edelman RR, Warach S. The ischemic penumbra: operationally defined by diffusion and perfusion MRI. *Neurology* 1999;53(7):1528-1537.
68. Wycliffe ND, Choe J, Holshouser B, Oyoyo UE, Haacke EM, Kido DK. Reliability in detection of hemorrhage in acute stroke by a new three-dimensional gradient recalled echo susceptibility-weighted imaging technique compared to computed tomography: a retrospective study. *J Magn Reson Imaging* 2004;20(3):372-377.
69. Santosh C, Brennan D, McCabe C, Macrae IM, Holmes WM, Graham DI, Gallagher L, Condon B, Hadley DM, Muir KW, Gsell W. Potential use of oxygen as a metabolic biosensor in combination with T2*-weighted MRI to define the ischemic penumbra. *J Cereb Blood Flow Metab* 2008;28(10):1742-1753.

70. Park SH, Moon CH, Bae KT. Compatible dual-echo arteriovenography (CODEA) using an echo-specific K-space reordering scheme. *Magn Reson Med* 2009.
71. Kidwell CS, Alger JR, Saver JL. Beyond mismatch: evolving paradigms in imaging the ischemic penumbra with multimodal magnetic resonance imaging. *Stroke* 2003;34(11):2729-2735.
72. Murphy BD, Fox AJ, Lee DH, Sahlas DJ, Black SE, Hogan MJ, Coutts SB, Demchuk AM, Goyal M, Aviv RI, Symons S, Gulka IB, Beletsky V, Pelz D, Hachinski V, Chan R, Lee TY. Identification of penumbra and infarct in acute ischemic stroke using computed tomography perfusion-derived blood flow and blood volume measurements. *Stroke* 2006;37(7):1771-1777.